# PEMFC performance decay during real-world automotive operation: evincing degradation mechanisms and heterogeneity of ageing

*Elena Colombo*[*1], *Andrea Baricci*[1], *Andrea Bisello*[1], *Laure Guetaz*[2], *Andrea Casalegno*[1]

[1]Politecnico di Milano, Department of Energy, Via Lambruschini 4, 20156, Milano, Italy

[2] Université Grenoble Alpes, CEA, LITEN, 17 Rue des Martyrs, 38054, Grenoble, France

[*] Corresponding author: elena.colombo@polimi.it

## Abstract

A long-term dynamic load cycle is performed on state-of-the-art membrane electrode assemblies, aiming to evaluate the degradation mechanisms of Polymer Electrolyte Membrane Fuel Cell under real-world automotive operations. The load cycle, adapted from the stack protocol defined in H2020 ID-FAST European project, includes load, pressure and temperatures cycling. Events that recover the temporary decay are included, specifically procedures classified in short-stops, cold-soaks, long-stops. *Operando* voltage and current distribution are measured through a segmented hardware, combined to local *in-situ* electrochemical characterization. Investigation is supported by scanning and transmission electron microscopy analysis, performed at different locations along-the-flow-field.

Reversible degradation weights from few to 20 mV and changes local current distribution, mostly at air-inlet, since the dry-out of ionomer. Cycle efficiency decreases of 3%-9%: the largest irreversible performance losses are observed at air-inlet, while middle-region is the least impacted. Cathode catalyst layer and membrane are the most aged components: platinum active surface area drops in 200-400 hours, because of electrochemical Ostwald ripening mechanism, and stabilizes around 62%-67% of initial value. Polymer membranes report ageing compatible with mechanical stress that causes localized thinning, increasing hydrogen crossover. Decay of ionomer in the catalyst layer is discussed, which would consistently explain alterations of mass transport resistance.

## Keywords

Polymer Electrolyte Membrane Fuel Cell, Dynamic load cycle, Local degradation, Automotive, Catalyst layer durability, Degradation mechanism

## 1. Introduction

Polymer Electrolyte Membrane Fuel Cells (PEMFC) are suitable for transport application in order to accelerate decarbonization. Nevertheless, PEMFC technology still needs to overcome some limitations with the aim of reaching sufficient targets[1] that would allow its widespread commercialization. One of the most challenging aspects to work on is durability: improving stability and operation requires the good knowledge of the occurring degradation processes. Even though the mechanisms that rule PEMFC ageing have been extensively studied[2,3], their contribution in the real-world should be clarified.

A first approach for the experimental study of single cell degradation consists in adopting Accelerated Stress Tests (AST)[2,4], with the aim of enhancing specific degradation mechanisms of MEA, in particular of electrodes and membrane, recognized as the most critical layers[5]. For assessing cathode catalyst durability, the loss of the Electrochemical Active Surface Area (ECSA) is promoted through particle growth[6] due to dissolution/redisposition (electrochemical Ostwald ripening) and migration or through particles detachment because of support corrosion. These processes depend on many factors, like potential limits[7,8], temperature[7,9] relative humidity (RH)[9,10], potential sweeps and dwell times[8,11], but also material properties as the particle size distribution[12] and support characteristics[13]. Dedicated ASTs[14] have been developed for studying perfluorosulfonic acid (PFSA) membranes ageing as well. The roots of ionomer degradation are identified in chemical decomposition[15,16], promoted by radical species, and in mechanical degradation[17,18], due to fatigue stress related to thermal and water content fluctuations. Similar processes[19–21] affect the morphological structure of ionomer inside the electrodes, resulting in its rearrangement, agglomeration and thinning. Some studies[22,23] suggested catalyst activity suppression, increase of local thin film resistance and loss of proton conductivity due to such phenomena, but the full comprehension of this component alterations is far to be reached.

In addition to ASTs, operations closer to real systems were studied at single cell level, implying by nature heterogeneous operating conditions over the active area[24]; such non-uniformity has a relevant impact on PEMFC lifetime[25–27]. Quantitative information about the physical phenomena that locally rise can be obtained through segmented cell[28,29]. Most of the literature that adopted this experimental approach is focused on off-design events, like fuel starvation[30,31] and air start-ups[32,33], or it is devoted to study MEA heterogeneous functioning but at fixed operating parameters[34]. In a few works, cycles of operational conditions were introduced, even though most of the times they were restricted to stand-alone quantities, as load[35] and relative humidity[36], or aim to investigate single components, as membrane[37]. The mentioned literature was fundamental to move towards a deeper comprehension of the heterogeneous ageing under dynamic modes.

However, the correlation to real-world automotive lifetime is still challenging[38–40]; anyway, quantifying the performance losses and their origin under a representative functioning is a key frontier. It should be noted that current systems implement operating strategies which must be considered in degradation studies, to orientate R&D activities to those challenges that are still open. In this framework, the present paper aims at providing an insight into local MEA alterations, by applying a long-term, complete degradation test and combining different measurement techniques to reach a wide understanding of the occurring mechanisms. The adopted program synchronously cycles the most relevant operational parameters (pressure, temperature, dew points and load), keeping a strict relation to real-world MEA working. The single cell protocol was adapted from the stack test proposed in the H2020 European ID-FAST project[41], the design of which was based on a road fleet dataset. In addition, the local study is ensured by the adoption of a macro-segmented hardware[25,42,43] The ageing is evaluated by: (*i*) cell voltage decrease, both *operando* and through polarization curves; (*ii*) local distribution of currents; (*iii*) electrochemical techniques like cyclic and linear sweep voltammetry for measuring ECSA, hydrogen crossover and shorting resistance and Electrochemical Impedance Spectroscopy (EIS); (*iv*) mass transport resistance evolution; (*v*) *post-mortem* analysis based on scanning (SEM) and transmission electron microscopy (TEM). *In-situ* and *ex-situ* local degradation of electrodes and membrane is correlated to the stressors observed under the protocol application with the purpose of clarifying the role of the degradation mechanisms. Three state-of-the-art MEAs were tested for 1000 operating hours each and what obtained compared to guarantee results reliability and extend generality of conclusions.

## 2. Experimental methodology

### *2.1. Material*

The experimental analysis was performed on three commercial Membrane Electrode Assemblies (MEAs) to consolidate results generality and evidence differences. Each MEA consists of (*i*) an automotive commercial Catalyst Coated Membrane (CCM) using Pt/C catalyst both at anode and cathode, supplied by different manufacturers, which characteristics are included in Table 1; (*ii*) gas diffusion layers (Freudenberg GDL H14CX483). The samples compression was obtained using rigid gaskets in PTFE aiming to 80% mechanical compression. The active area was delimited using few µm-thick Mylar sub-gaskets.

*Table 1 CCMs tested in the segmented hardware (25 $cm^2$) under single cell driving cycle protocol. Characteristics were declared by the manufacturers or obtained through SEM images. Pt roughness factor at BoT is calculated from $H_2/N_2$ Cyclic Voltammetry.*

| Characteristic | Units | CCM A | CCM B | CCM C |
|---|---|---|---|---|
| Cathode Catalytic Loading | [mg $cm^{-2}$] | 0.4 | 0.5 | 0.4 |
| Anode Catalytic Loading | [mg $cm^{-2}$] | 0.08 | 0.1 | 0.1 |

| | | | | |
|---|---|---|---|---|
| Membrane thickness | [µm] | 15 reinforced + radical scavenger | 18 reinforced + radical scavenger | 18 reinforced + radical scavenger |
| Cathode Catalyst layer thickness | [µm] | 10 | 15 | 10 |
| Anode Catalyst layer thickness | [µm] | 7 | 5 | 3 |
| Carbon support | | graphitized | graphitized | - |
| Roughness factor at BoT | [$cm^2_{Pt}$ $cm^{-2}_{geo}$] | 165 | 201 | 207 |

### *2.2. Hardware and setup*

A 25 $cm^2$ segmented hardware is used, permitting an analysis on four macro-regions of the cell through an active localized control. The cell active area attributed to each segment from 1$^{st}$ to 4$^{th}$ is equal to 5.83 $cm^2$, 5.80 $cm^2$, 7.65 $cm^2$ and 5.72 $cm^2$. A complete electrochemical characterization of each region is ensured. The reader could refer to previous works[44][43][33] for a more detailed description of the segments geometry and of the setup functioning. Flow field features a triple serpentine channel. Under galvanostatic operation, the total current is imposed: aiming to a uniform MEA voltage, the single segment current is individually controlled through a modular electronic load (multichannel Chroma® 63610-80-20). This configuration identifies the instantaneous contribution of each segment to the overall current.

The testing station is designed to dynamically control the operating conditions. The mass flow rates are defined by the current through stoichiometries. The gas flow is regulated by flow meters (Brooks® 5850s). The level of humidification is fixed by water bubblers (Fuel cell tech®) that keep the desired dew point. Two bubblers are used for both anode and cathode side; this configuration allows to switch rapidly between the different dew points of the protocol, as described in the load cycle section. Outlet reactants pressures are regulated using electronically controlled backpressure valves (Equilibar® LF Series), installed at the outlet manifolds of the cell hardware. Pressure level is measured by pressure transducers (GE® Unik 5000) connected both to anode and cathode, at inlet and outlet. Data acquisition system is based on National Instrument® DAQmx interface and a custom developed LabView® interface, integrating the setup in a comprehensive platform.

### *2.3. Break-in procedure*

A break-in procedure was adopted prior to the ageing protocol application. The MEA is conditioned at 65 °C, 100% RH, ambient pressure and stoichiometry of 2/4 at anode and cathode respectively: the current density was varied between 0.2 and 0.8 A $cm^{-2}$ every 120 s. The MEA performance stability checked every 40 min at 0.5 A $cm^{-2}$. The procedure lasted ~17 hours.

### *2.4. In-situ characterization*

To monitor the degradation of MEAs during the application of the driving cycle protocol, polarization curves, cyclic voltammetry (CV), linear sweep voltammetry (LSV) and electrochemical impedance spectra (EIS) were measured. This *in-situ* characterization allowed to obtain both global and local information and it was introduced every 200 operating hours of the ageing protocol. Cyclic voltammograms were recorded between 0.075 V – 0.6 V using $H_2$-rich anode as reference electrode, with a scan rate of 50 mV $s^{-1}$, a temperature of 30 °C, fully humidified gas flows. On the anode side, pure hydrogen flow was set equivalent to 0.06 NL $min^{-1}$, while the nitrogen flow on the cathode side was set to zero during the measurement. The electrochemically active surface area was calculated by the H-desorption area, as an average on four scans, using a specific charge of 210 µC $cm^{-2}$. LSV was used for estimating hydrogen crossover by identifying the i-V linear dependence and extrapolating the value of current density at null voltage. LSV was recorded between 0.05–0.6 V with a scan rate of 1 mV $s^{-1}$, 80 °C and fully humidified streams, under different pressure conditions, in order to evaluate the crossover current as a function of hydrogen partial pressure and/or absolute pressure. Every time the crossover current is reported, pressure conditions are specified. In addition, the inverse of the slope in the linear 0.3–0.6 V region provides an estimation of the shorting resistance.

A set of polarization curves was adopted. Table 2 summarizes the operative parameters.

*Table 2 Polarization curve operating conditions used for MEAs characterization at long stops, every 200$^{th}$ cycles of the load cycle protocol. Adopted stoichiometries are, for anode and cathode respectively: (i) 2/20 for oxygen polarization (ii) 2/4 for all the other conditions.*

| Name | T Cell °C | Dew point Cathode °C | Dew point Anode °C | RH Cathode % | RH Anode % | $P_{,out}$ Cathode $kPa_{,abs}$ | $P_{,out}$ Anode $kPa_{,abs}$ | $x^{dry}_{O2}$ % |
|---|---|---|---|---|---|---|---|---|
| oxygen | 80 | 80 | 80 | 100 | 100 | 230 | 250 | 100 |
| reference | 80 | 80 | 80 | 100 | 100 | 230 | 250 | 20.9 |
| ID-FAST | 68 | 43 | 58 | 30 | 63.5 | 280 | 300 | 20.9 |

Each current density of the polarization curve was held for 180 s and averaged over the last 120 s, considering the progress from high to low currents. During each polarization curve protocol, EIS was measured in galvanostatic mode at 0.8 A $cm^{-2}$ and 0.4 A $cm^{-2}$. A total of 40 frequencies was applied, in the range from 100 mHz to 20 kHz.

A limiting current test was arranged for computing the oxygen mass transport resistance, following the approach of Baker et al[45]. Three dilutions were tested: 1%, 2% and 3% of $x^{dry}_{O2,in}$ in nitrogen, at pressures $p_{A,in/C,in}$=220/200 kPa, 270/250 kPa, 370/350 kPa. Hydrogen flow was kept constant at 1.0 NL $min^{-1}$, while cathode flow at 3.0 NL $min^{-1}$. The cell voltage was held for 3 minutes

at 0.4 V, then lowered to 0.3, 0.25 and 0.2 V, held 3 minutes per each, where the limiting current was recorded and averaged. From the limiting current, the oxygen mass transport resistance ($R_{MT}$) is estimated according to Equation 1:

$$R_{MT}\left[\frac{s}{cm}\right] = 4F\frac{x_{O_2}^{dry}}{i_{lim,measured} + i_{crossover}(p)}\frac{p - p_w}{RT} \quad (1)$$

where $p$ is the total gas pressure, $p_w$ is the water vapour pressure and $x^{dry}_{O2}$ is the oxygen molar fraction, computed as the logarithmic average between inlet and outlet:

$$x_{O_2}^{dry} = \frac{x_{O_{2,in}}^{dry} - x_{O_{2,out}}^{dry}}{\ln\left(\frac{x_{O_{2,in}}^{dry}}{x_{O_{2,out}}^{dry}}\right)} \quad (2)$$

The dry oxygen mole fraction at outlet is computed from the value at inlet and the consumed oxygen because of the drawn current:

$$x_{O_{2,out}}^{dry} = x_{O_{2,in}}^{dry} - \frac{1}{\dot{V}}\frac{i_{lim}\,Area}{4\,F}\,\frac{RT}{p} \quad (3)$$

Where $\dot{V}$ is the volumetric flow rate [$m^3\ s^{-1}$] and *Area* is the active area (25 $cm^2$).

### *2.5. Local ex-situ analysis: scanning and transmission electron microscopy*

Samples were cut from CCM A and B, both fresh and aged under load cycle. For aged CCMs, cross-sections were taken at different positions along the flow field: at air-inlet, middle and outlet. After embedding in epoxy resin, cross-section samples were prepared by mechanical polishing until mirror-like surface. They were then observed by scanning electron microscopy. In addition, for the CCM B, thin slices (100 nm thick) of the cross-sections were cut using a LEICA ultramicrotome and analyzed by transmission electron microscopy.

SEM and TEM observations were respectively performed using a ZEISS-MERLIN field emission gun (FEG) microscope and a FEI-Titan Ultimate microscope equipped with both a Cs aberration probe and image corrector. For each sample, histograms of Pt nanoparticle (Pt NP) size distribution were built from TEM images. Pt nanoparticle sizes were measured manually. For obtaining the particle size distribution: (*i*) grey level threshold was applied to pictures; (*ii*) agglomerated particles were not taken into consideration; (*iii*) spherical nanoparticles only were considered, for which the geometric surface area (GSA)[46] was calculated from measured diameters according to Equation 4:

$$GSA\left[\frac{m^2}{g}\right] = \frac{6}{\rho_{Pt}}\frac{\sum_i d_i^2}{\sum_i d_i^3} = \frac{6}{\rho_{Pt}}\frac{1}{\bar{d}} \quad (4)$$

where $d_i$ indicates the diameter of the individual $i^{th}$ nanoparticle, $\rho_{Pt}$ is the density of platinum (21.45 g $cm^{-3}$), $\bar{d}$ is the volume/area average diameter.

### *2.6. Dynamic load cycling protocol*

The ageing protocol performed in this study is adapted from the stack driving cycle developed in the European ID-FAST project (H2020 id:779565). The ID-FAST consortium defined a representative drive cycle based on several hours of customer fleet data. It contains synchronous variation of temperature, pressure, relative humidity and load. These transitory conditions are obtained from PEMFC systems but are challenging to reproduce on a testing station at laboratory scale. Information about the methodology adopted for deriving the durability test program are in project documents[41].

In this work, a segmented single cell (Figure 1.C) was operated in a counter-flow configuration: air flow gets into the first segment, while hydrogen inlet is located at the fourth. The adopted stoichiometry is 1.4 and 1.6 for anode and cathode respectively. The dynamic cycle is divided into two parts: a low load and a high load operation, represented in Figure 1.A. The transition from the two operational modes occurs at minute 47. The low load part lasts for two-third of the operative cycle, while the remaining one-third is attributed to high load. The cell temperature is accurately control: a value of 71 °C is kept over the active area under low load operation and it increases up to 90 °C through a ramp at high load (see Figure 1.A). Absolute outlet pressure is regulated at both anode and cathode. Constant values are kept during low load: 190 kPa and 140 kPa respectively. During the transition from low to high load, the pressure increases up to 300/280 kPa. Pressure transitions should not exceed 10 seconds. Table 3 summarizes the different pressures associated to specific current setpoints of the protocol. Dew point variations of the feeding gases are obtained through the gas switch between different bubblers, two located at each cell side. The dew points are set in order to keep inlet relative humidity close to 30% at cathode and 50% at anode for the two temperatures of 71 and 90 °C. Since in high load the cell temperature is not fixed but follows a ramp, the relative humidity varies during these transitions.

*Table 3 Operative parameters of the driving cycle protocol used for testing single cells. The total operating time of each cycle is equivalent to 3600 s (stops excluded): the second column indicates the operating time fraction for which the cell is run at the conditions specified in the row. Points indicated with (*) are involved in the cell temperature ramp, as shown in Figure 1.A.*

| Cycle point | Current density [A cm$^{-2}$] | Operating time [%] | $P_{anode,out}$ [kPa] | $P_{cath.,out}$ [kPa] | $\lambda_{anode}$ | $\lambda_{cathode}$ | Tcell [°C] | $T_{dew\ anode}$ [°C] | $T_{dew\ cathode}$ [°C] |
|---|---|---|---|---|---|---|---|---|---|
| 1 | 0.095 | 49.58% | 190 | 140 | 1.4 | 1.6 | 71 | 58 | 43 |
| 2 | 0.247 | 18.61% | 190 | 140 | 1.4 | 1.6 | 71 | 58 | 43 |
| 3 | 0.589 | 11.11% | 190 | 140 | 1.4 | 1.6 | 71 | 58 | 43 |
| 4 | 1.273 | 7.92% | 275 | 248 | 1.4 | 1.6 | 71(*) | 72 | 57 |
| 5 | 1.748 | 12.78% | 300 | 280 | 1.4 | 1.6 | 90(*) | 72 | 57 |

Figure 1.B depicts the current density imposed during each cycle (galvanostatic control). As an example, the Beginning of Test (BoT) voltage response of CCM A is inserted. Each cycle of the protocol requires one hour of operation, indicated as operating time. In addition, several stop conditions were included. First, the cycle is interrupted every 30 minutes by a short stop. During the 5-minutes short stop, hydrogen is supplied while the air flux is closed and a resistive load is applied in order to actively reduce the cell voltage, avoiding open circuit (OCV). The cycle is repeated five times, after which a cold soak is introduced. The cold soak includes the cell cooling down and lasts two hours. Finally, every 200$^{th}$ cycle, a long stop of 12 hours is integrated and a recovery procedure is applied. It consists in performing cyclic voltammetry between 0.07–1.20 $V_{RHE}$ ten times, with a scan rate of 100 mV $s^{-1}$, at 30 °C. Thereafter, the electrochemical and performance characterization is carried out. Further details about stop protocols are reported in Appendix. A summary of the testing procedure is included in Figure 1.D, while Figure 1.E evidences the fraction of total time (operating time and stops) spent at each cycle point.

Figure 1.B shows also the High Frequency Resistance (HFR) measured at 1 kHz during a cycle. This quantity provides an indication of the humidification state of the MEA and varies with the local position and the operating point. At low load, the inlet operates such dry to result in the highest measured values. When the current setpoint is increased, the product water quickly hydrates the membrane and rapidly reduces HFR. In the middle and in the outlet areas, drying is prevented by accumulation of product water along the flow field, exhibiting progressively lower values. As the operation moves from low to high load, water content increases, because of the increasing pressure and current. A clear HFR reduction is visible during the transition at minute 47. Then, coming back from high to low load, impedance increases suddenly (time >65 min): the most severe dehydrated conditions are reached because of the low current supplied when the cell temperature is reducing but the electrode is still hot since the heat generated during the previous high current operation. Notably, segment 1 undergoes the widest oscillations during each cycle.

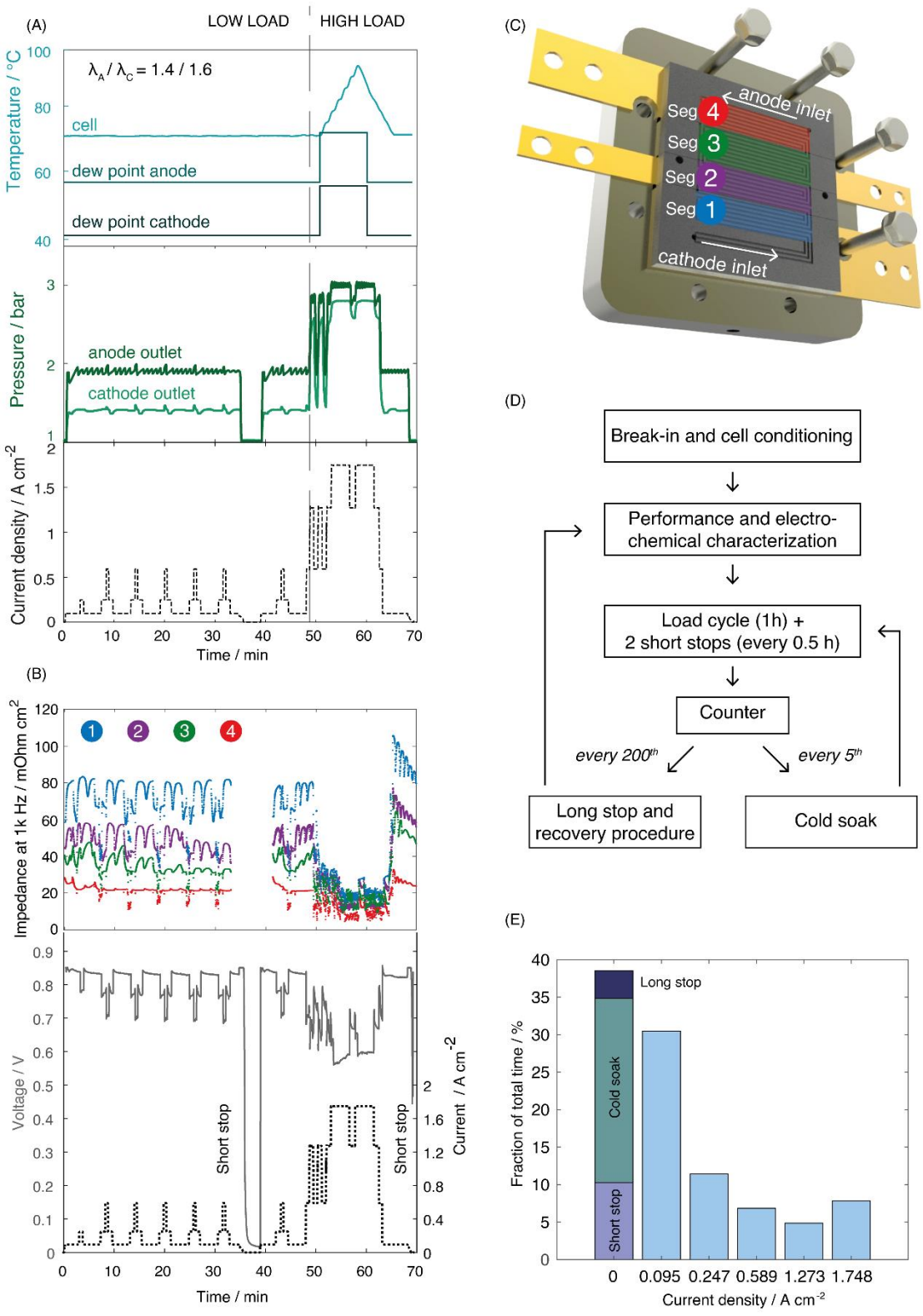


*Figure 1(A) Operating parameters applied during each cycle of the ageing protocol: current densities, outlet pressures (expressed as absolute values), cell temperature and bubblers dew point. Two short stops are introduced for every operating hour (correspondent to 0 A cm$^{-2}$); (B) Relevant quantities measured during a cycle for CCM A, at BoT: voltage profile and impedance at 1 kHz. This second information is collected for each local region of the MEA, thanks to the hardware scheme reported in Figure 1.C; (C) Four macro-segmented hardware adopted for load cycle protocol application. Gas feedings are in counter-flow configuration. Segment 1 corresponds to air-inlet, segment 4 to outlet; (D) Schematized representation of the durability protocol; (E) Time spent at each specific current of the durability protocol: fraction with respect to the total testing time (stops included).*

## 3. Results and discussion

### *3.1. Performance loss induced by load cycling protocol: operando analysis*

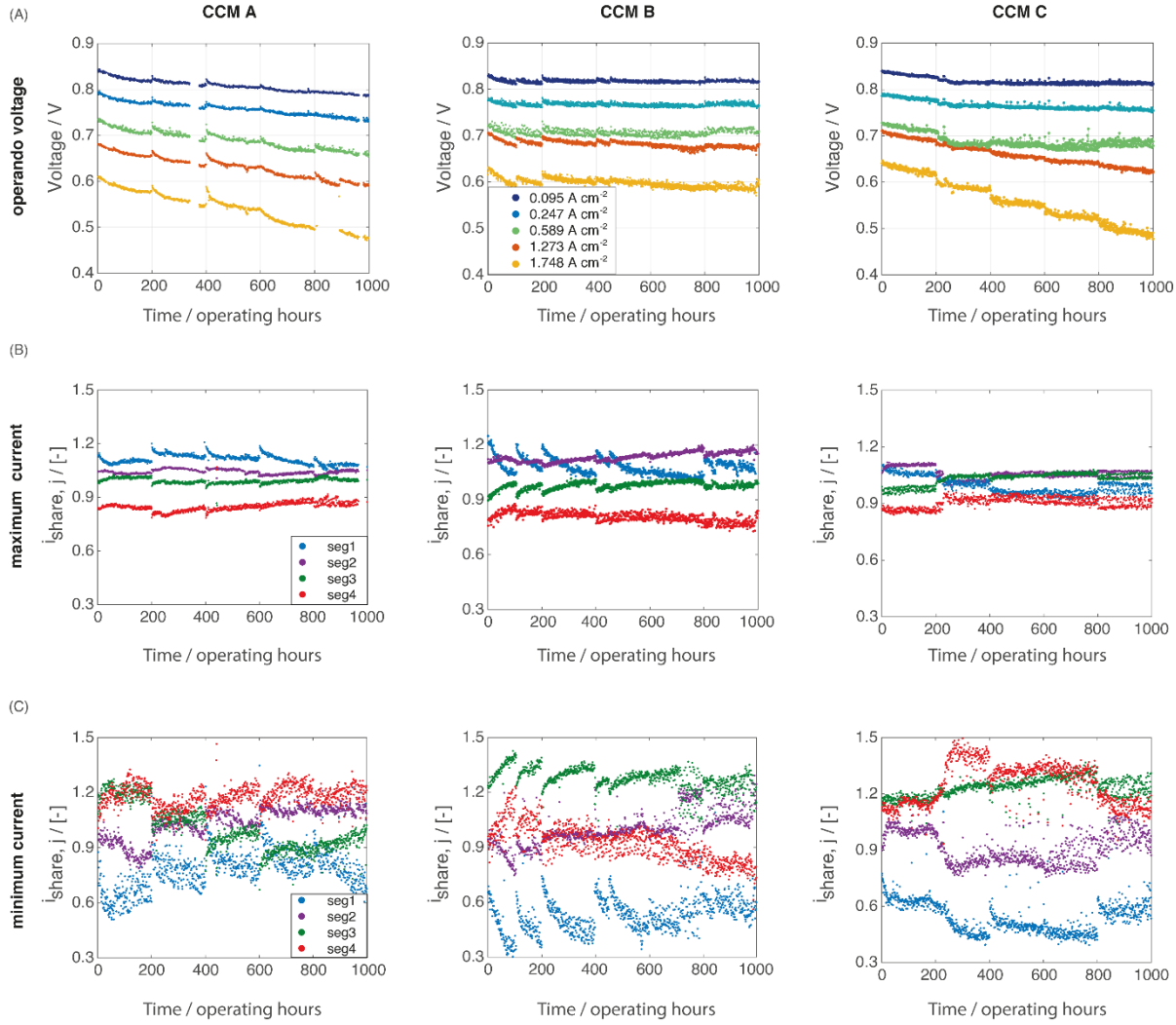


*Figure 2 (A) Operando voltage at different current setpoints of load cycle. Results for the three different tested CCMs are compared (CCM A, B, C, see Table 1); (B) Current distribution among the segments at maximum current setpoint of load cycle (1.748 A cm$^{-2}$) and related evolution over time. Each contribution is expressed as the ratio of the current density generated by the segment to the imposed cell setpoint (overall current density). (C) Current distribution among the segments at minimum current setpoint of driving cycle (0.095 A cm$^{-2}$) and related evolution over time. Each contribution is expressed as the ratio of the current density generated by the segment to the imposed cell setpoint (overall current density). Definition of $i_{share}$ is provided by Equation 5.*

The voltage measurement performed during the cycle was averaged for each of the five points included in Table 3, to compare samples degradation. Since the protocol is controlled in galvanostatic mode, changes in the cell voltage response could be checked alongside operation. The resulting evolution in time is included in Figure 2.A and indicated as operando voltage profile. The performance of the different CCMs is quite comparable at zero time and it ranges from 0.85 V (all the CCMs) at 0.095 A cm$^{-2}$ to 0.61 V (CCM A)/0.63 V (CCM B)/0.64 V (CCM C) at 1.748 A cm$^{-2}$. On the other hand, evolution in time differs. From this chart, an information that briefly summarizes the global cell losses induced by automotive-like operations is computed. Simple rates of voltage decrease are defined through linear fitting of the profiles, determined by removing the first 100

operating hours, where the trend is strongly non-linear and after which linearity assumption is considered reasonable. The obtained abridged degradation rates are included in Table 4 and expressed equivalently in µV $h^{-1}$, where the time is the operative, or in µV $cycle^{-1}$. For all the CCMs, the rate of loss depends on current density and it monotonically increases with it. CCM A shows a rate of loss ~4 times larger than CCM B at the highest current and even ~15 times larger at minimum current. CCM C shows a different behaviour: at the highest current, the loss is close to CCM A, while at low/middle currents it is an intermediate between CCM A and B. CCM B is thus proved as the most resistant to degradation among those tested, in particular at high currents. It is observed that such CCM present the highest load (0.5 mg $cm^{-2}$ against 0.4 mg $cm^{-2}$ of the other MEAs), but it has a comparable roughness factor to CCM C (see Table 1). The explanation of the observed different ageing was researched by quantifying and combining the evolution of different parameters, *e.g.* ECSA, crossover current and oxygen mass transport resistance, as discussed in the following sections.

*Table 4 Operando rate of voltage loss at different current density setpoints of the load cycle protocol. Values are reported for different CCMs and computed as a linear fitting on the voltage profile in the range 100-1000 operating hours.*

| Cycle current point [A $cm^{-2}$] | Rate of voltage loss during driving cycle protocol [µV $h^{-1}$] | | |
|---|---|---|---|
| | CCM A | CCM B | CCM C |
| 0.095 | 34.0 | 2.4 | 15.9 |
| 0.589 | 55.1 | 13.5 | 19.1 |
| 1.273 | 81.4 | 21.9 | 43.3 |
| 1.748 | 127.0 | 31.7 | 136.1 |

The adoption of a segmented cell hardware allows to investigate spatial current distribution. Table 5 summarizes how the current is locally provided at BoT. In low load operation, described in the protocol section, the middle region is the most performing, followed by the outlet. The inlet area is instead hindered by the dry operating conditions, resulting from the low relative humidity of gas feeding and by the low current setpoints. In high load, the current distribution follows instead the cathode flow direction. The higher loads allow for a better humidification of the inlet region, and the current distribution is controlled by the oxygen partial pressure, that makes the outlet suffer. Since low load operation lasts twice high load, the middle region (seg2, seg3) is the part of MEA that overall provides the largest contribution. Few differences are observed between samples; CCM A suffers less the low relative humidity at air-inlet than the other samples, which could be ascribed to properties of the polymer membrane.

*Table 5 Current density distribution computed for each MEA region and specific material at Beginning of Test. Values are obtained as an average over the low load operation of a cycle and over the high load operation of a cycle. For this computation, the first 5 operating hours have been taken into account.*

| | Average current density [A cm$^{-2}$] at Beginning of Test | | | | | | | | | | | |
|---|---|---|---|---|---|---|---|---|---|---|---|---|
| | CCM A | | | | CCM B | | | | CCM C | | | |
| | Seg1 | Seg2 | Seg3 | Seg4 | Seg1 | Seg2 | Seg3 | Seg4 | Seg1 | Seg2 | Seg3 | Seg4 |
| Low Load Operation | 0.143 | 0.179 | 0.203 | 0.181 | 0.122 | 0.187 | 0.214 | 0.181 | 0.129 | 0.180 | 0.207 | 0.189 |
| High Load Operation | 1.167 | 1.107 | 1.042 | 0.922 | 1.190 | 1.150 | 0.985 | 0.896 | 1.110 | 1.124 | 1.013 | 0.967 |
| Overall cycle | 0.389 | 0.400 | 0.403 | 0.357 | 0.378 | 0.416 | 0.398 | 0.326 | 0.364 | 0.406 | 0.399 | 0.326 |

The current distribution is changing in time, as a consequence of reversible and irreversible losses. The evolution could be tracked for each point of the protocol through the local current density fraction. For sake of brevity, only two cases, correspondent to minimum and maximum cycle current, are provided in Figure 2.B and 2.C. This *operando* local quantity was calculated as:

$$i_{share,j}\,(t) = \frac{i_{local,j}\,(t)[A\ cm^{-2}{}_j]}{i_{total}\,[A\ cm^{-2}]} \qquad (5)$$

where *j* is referred to a specific segment. The current density (*i*) fraction evolves in time, according to both temporary and permanent changes. It is recognized that the performance degradation comprises two kinds of processes, one reversible and one irreversible[47,48]. The adoption of a load cycle that contemplate different stops conditions allows to partially recover the reversible component. Short stops are expected to remove the platinum oxides formed over the catalyst surface at high potentials, by decreasing the cell voltage to approximately 0 V[49,50]. In addition, the reduction of cell temperature during cold soaks would allow to increase humidity, reducing ionomer stress and favoring recovery[51]. Even though the largest part of the reversible losses is expected to be recovered frequently, long stops seem to provide additional benefits. Their impact is evinced every 200$^{th}$ operating hours: voltage profile improves from few to ~20 mV. Moreover, the current density distribution significantly modifies while operating over 200 cycles: the alteration is mostly evident for CCM B at minimum current (Figure 2.C). The largest temporary drop was measured for air-inlet: $i_{share,1}$ decreases from 0.74 to 0.42 between 201-400 hours and came back to 0.70 at hour 401, thanks to the combined application of long stop and recovery protocol. *Operando* reversible loss is compensated by a boosted input of the middle region, in particular of segment 3. A similar impact is observed for CCM A at high load operation, while CCM C seems unaffected by the phenomenon, the intensity of which results material dependent. The reversible performance drop at cathode inlet might

be associated to drying-out of the ionomer in the catalyst layer and/or membrane. The de-hydrated conditions are supposed to be responsible for catalyst poisoning through ionomer because of an increase in anion adsorptivity under low RH[52]. The effect was also proved in literature[53] in case of low surface area support, as graphited carbon. The combination of longer periods at higher relative humidity during long stops and the application of potential sweeps to 1.2 V, appeared as an effective method for removing that part of reversible ageing that was not cleaned during short stops and cold soaks. Anyway, further understanding of recovery under drive cycle will require future dedicated works.

As regards irreversible changes between beginning and end of test, variations of current distribution are detected at high load for segment 1, followed by segment 4. For all the materials, middle region is the least affected at highest current. On the other hand, segment 3 decreases its contribution at low load, mostly for CCM A: $i_{share,3}$ largely reduces from 1.20 to 0.95 over 1000 hours. The underlying degradation, responsible of these altered performances, is addressed in the following sections.

### *3.2. Platinum catalyst degradation*

The platinum active surface area was computed from cyclic voltammetry, every 200$^{th}$ hours. At 1000 operating hours, an overall loss of 41% is identified for CCM A, 35% for CCM B and 32% for CCM C. ECSA profile in time is close for all the CCMs and is well described by the exponential decay of Equation 6:

$$S = S_{min} + (1 - S_{min})e^{-\lambda x};\ S = \frac{ECSA}{ECSA_{BoT}} \qquad (6)$$

*S(x)* is the normalized surface area and is a function of the *x* number of protocol cycles, equivalent to the operating hours. λ is a proportionality constant that correlates the rate of surface area decay to the remaining area that could be lost. In addition, it emerges a minimum surface area, $S_{min}$, which seems less susceptible to degradation. This description was already adopted in other works that studied electrocatalyst ageing under voltage cycling[8,11,54]. The parameters $S_{min}$ and $\lambda$ are regressed over the experimental data and their values collected in Table 6. The fitting was included in Figure 3. The largest decay is in the first 200 operating hours. After 400 hours, ECSA becomes more stable, subjected to minor variations. The underlying mechanism responsible of this measured loss was investigated through *post-mortem* analysis, based on SEM and TEM characterization.

*Table 6 Parameters of Equation 6 used for describing ECSA decay under the application of load cycle protocol on the three tested CCMs. Values are regressed over experimental data by minimizing the mean square error.*

| | CCM A | CCM B | CCM C |
|---|---|---|---|
| $S_{min}$ | 0.62 | 0.65 | 0.67 |
| $\lambda$ | 4.1e-3 | 5.1e-3 | 4.7e-3 |

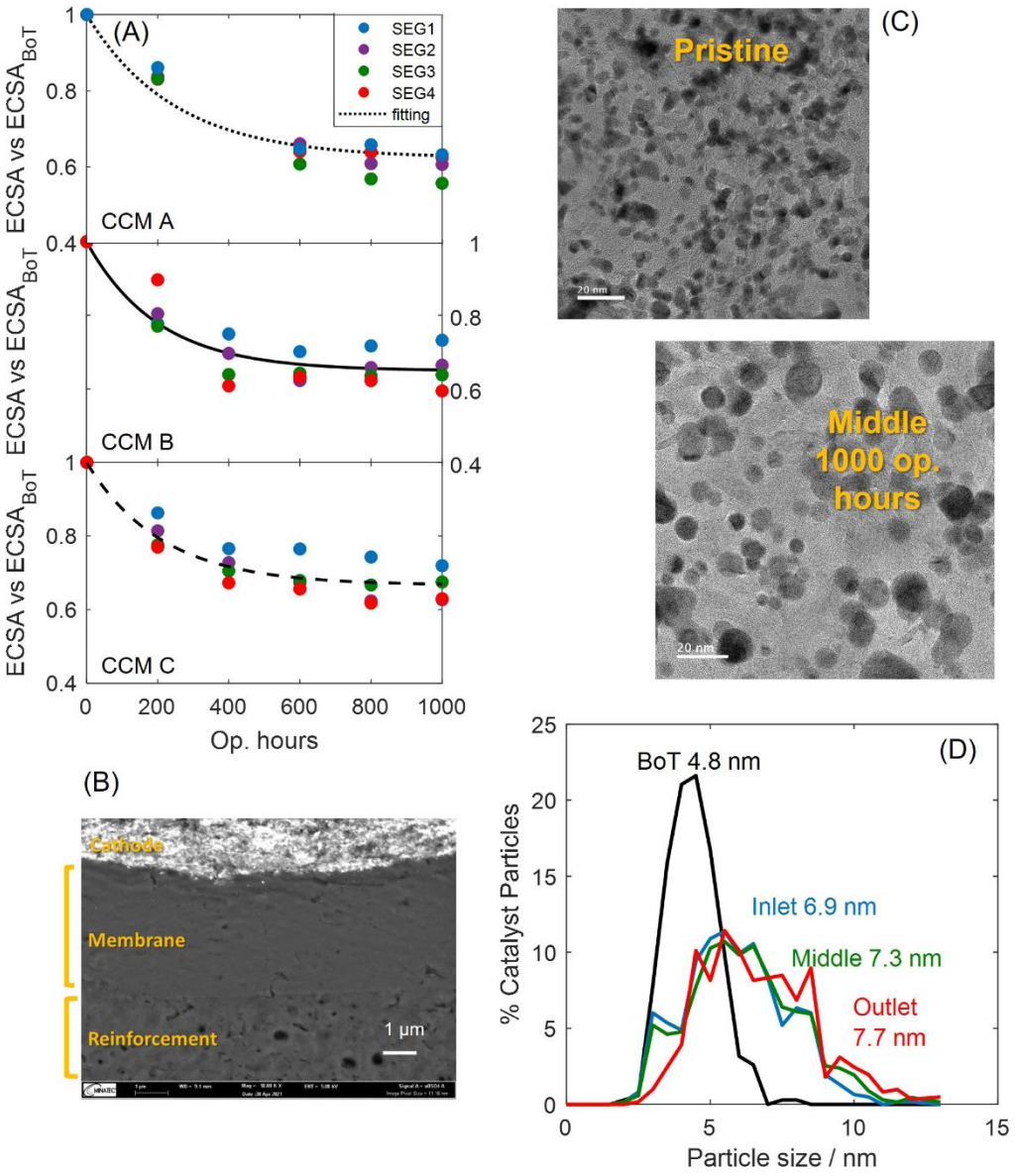


*Figure 3 (A) ECSA decay as a function of the operating hours for the three CCMs tested under the load cycle protocol. Average information is provided through the overall fitting, while local ECSA is obtained by the local Cyclic Voltammetry, measured at every long stop characterization; (B) SEM image of CCM A after 1000 operating hours: focus on membrane that evidences the limited Pt precipitation into ionomer. Middle region along the flow field direction is shown; (C) Representative TEM images for the after break-in CCM B and for middle region of the same CCM after 1000 operating hours of load cycle; (D) Particle size distributions for CCM B, evaluated after break-in procedure (BoT) and after 1000 operating hours of load cycle, at inlet region (seg1, in blue), middle region (between seg2 and seg3, in green) and outlet region (seg4, in red). Values of the average volume/area diameters are included too.*

*Table 7 Table that summarizes the results of TEM images analysis carried out for CCM B, both for after break-in and aged MEA, under 1000 load cycles. Local information (air-inlet, middle and air-outlet) are provided. The table includes counted particles, as well as the obtained geometric surface area and average diameter. Only spherical and not agglomerated particles have been considered into counting. Results are compared to ECSA computed through local Cyclic Voltammetry.*

| MEA B region | Counted particles | GSA [$m^2/g$] | Volume/area average diameter ($\bar{d}$)[nm] | ECSA from CV [$m^2/g$] | Utilization factor [-] | GSA loss [%] | ECSA loss [%] |
|---|---|---|---|---|---|---|---|
| AFTER BREAK-IN | 347 | 58.70 | 4.8 | 40.1 | 0.68 | - | - |
| INLET | 615 | 40.59 | 6.9 | 29.1 | 0.72 | 30.9 | 27.4 |
| MIDDLE | 672 | 38.39 | 7.3 | 26.3 | 0.69 | 34.6 | 34.4 |
| OUTLET | 613 | 36.15 | 7.7 | 25.4 | 0.70 | 38.4 | 36.7 |

Figure 3.C shows TEM images of the cathode Pt nanoparticles of the after-break-in and the aged CCM B (middle area), which reveal that the size of nanoparticles largely increased after the ageing test. To construct the cathode Pt particles size distributions in the different samples (Figure 3.D) a large number of spherical particles as included in Table 7 was considered. Comparison of the histograms shows that the load cycle application broadened the extent of nanoparticles sizes in all the MEA regions. The Pt NPs diameter, which was initially in the range 2-7 nm, grew to be in the range 3-12 nm. At the opposite, TEM images of the anode revealed no important changes (Figure SI-1). From these histograms, the Pt GSA was calculated and an average diameter of Pt NPs was determined, as detailed in the experimental section. Cycled MEA presents a mean diameter approximately 1.5 times larger than fresh (from 4.8 to 7.3 nm) and nanoparticles with diameters lower than 5.5 nm disappeared during ageing. The result is aligned to Stariha et al.[4], who applied 1200 hours of U.S. DRIVE-FCTT wet-drive protocol, identifying a size increase from 4.5 to 7.4 nm.

Minor differences could be evinced among the CCM regions: the average diameter increases from inlet to outlet, and in the outlet area the amount of small particles (<4.5 nm) is lower, while greater the one of larger (>8.5 nm). The result could be explained by the higher relative humidity of the air outlet region, which enhances Pt ions mobility[10], compared to the drier air-inlet zone. Furthermore, degradation of Pt NPs during potential transients is strongly related to the oxidation state[55–57], also enhanced at high RH.

Pt utilization is obtained comparing GSA to the ECSA calculated from cyclic voltammetry, collected in Table 7. For fresh MEA, the Pt utilization value, equivalent to 0.68, is consistent to literature

data[58][46]. It is noteworthy that Pt utilization does not change significantly after degradation, resulting in range 0.69-0.72 for all the cases.

From these analyses, it is concluded that the electrochemical Ostwald ripening mechanism is the main driver for the active Pt surface area loss. During the potential cycles that characterize the driving protocol, smaller Pt particles dissolved and re-deposited upon larger. The particles are changed towards a symmetric shape and a good consistency between the loss of GSA and ECSA is identified. Their values deviate at air-inlet of only ~3.5%, while the deviation is even lower in the other regions. Some additional processes might happen that have an effect on the reported difference, as a variation in the contact between catalyst and ionomer. Furthermore, Figure 3.B illustrates the SEM image of CCM A. No Pt precipitation within the membrane is observed in all the regions along the channel direction (see also Figure 4). The absence of Pt band is probably consequence of a maximum voltage equivalent to 0.85 V, while OCV condition is avoided at all, in order to represent real stack mitigation strategies. At this maximum voltage, the amount of Pt ions that could diffuse and precipitate by the hydrogen crossover in the membrane is not significant. In addition, this potential limitation, combined to the adoption of corrosion resistant supports, prevented any relevant carbon corrosion. The absence of carbon oxidation was proved by *ex-situ* and *in-situ* analysis. In the range of measurement accuracy, no relevant catalyst layer thinning was observed as no CV alteration is detected in the potential range of double layer capacity[59]. The result is in agreement with literature works that keep voltage inferior to1 V[60,61].

However, the ECSA loss cannot be considered as the only driver for the observed performance degradation. Indeed, the different End of Test (EoT) performance among materials could not be explained considering the Pt active surface area only: the loss of performance of CCM B is much more limited rather than the other materials, while ECSA decay is comparable. Further mechanisms should be researched and they are the object of the next paragraphs.

### *3.3. Membrane degradation*

The membrane degradation was monitored *in-situ* through (*i*) hydrogen crossover, (*ii*) shorting resistance and (iii) High Frequency Resistance. Figure 4.A shows the crossover current measured setting outlet ambient pressure at cathode and 150 kPa at anode. For all the CCMs, the hydrogen crossover increased in time. In the meanwhile, the electronic short circuit resistance lowered (Figure SI-2). Clear differences among the CCMs are highlighted: the crossover current evolution indicates that CCM B is the most resistant to membrane degradation, since its value increase was the lowest, from 5 to 7 mA $cm^{-2}$ (+40%). At the opposite, CCM A is characterized by a very large increase of crossover current, evinced for segment 3 at 600 operating hours: a much higher value was identified at that time compared to BoT. Such a large change indicates that a membrane failure thus set-off in

the middle region. However, also the other segments, like seg.2 and seg.1, showed a large increase in crossover current later, in the range 800-1000 operating hours. This is an indication that the PEM damage became widespread over the cell active area, affecting all the MEA regions at the end of the test. At EoT, the average CCM A crossover of Figure 4.A is increased ~10 times (from 4 to 40 mA $cm^{-2}$) and for segment 3 it even increased ~18 times. This observation matches with the great loss of current contribution of air-middle ($i_{share,3}$) at the minimum cycle current density (Figure 2.C). At low currents indeed, the effects of shorting and hydrogen flux across the membrane weight a lot. In Figure 4.C, the CCM A hydrogen transport from anode looks dominated by the total pressure difference between the two sides, and not only by the partial pressure. This is concluded from the sudden increase in the crossover current when the absolute pressure at anode becomes greater than the cathode pressure. Such behaviour highlights the prevailing convective rather than diffusive origin of hydrogen flux[62] and indicates that the membrane failed because of pinholes formation.

CCM C results as an intermediate case, signed by a larger increase of crossover current than CCM B, but not showing a drastic failure as CCM A. Crossover current at pressurized conditions of Figure 4.A averagely increased from 5 to 13 mA $cm^{-2}$; the largest local current density is attributed to segment 3 at EoT (18 mA $cm^{-2}$). Notably, middle region is again subjected to the most severe alterations. The relative trend of membrane ageing for the different CCMs is consistent to the rate of voltage loss at the low current setpoint of load cycle, included in Table 4 (34.0 – 2.4 – 15.9 µV $h^{-1}$ for CCM A, B and C respectively at 0.095 A $cm^{-2}$): the performance at the lowest load is dominated by alterations of membrane permeability, if these occur.

As described in the dynamic protocol section, the air-inlet region was subjected to the widest variation of humidification over one-hour cycling, as well as to the lowest values of water content. One would expect a failure near air-inlet because of chemical degradation caused by exposure to low RH or because mechanical ageing driven by the amplitude of oscillations, but the most stressed membrane region was instead at air middle-outlet (seg 3). It should be observed that water content oscillations are widespread over the whole active area because of load and operating conditions cycling. In addition, middle region draws the highest average current density, mostly during the long-lasting low load operation (Table 4). Lai et al.[63] observed that the highest membrane mechanical stress alters the close-to-air-outlet region, by applying a current cycling protocol under low RH air feeding. Interestingly, they found a connection to the strongest water flux across the membrane. Also another work[37] presented the results of an AST that introduced simultaneous current and RH cycling: consistently to our findings, the MEA failed in the middle-outlet zone.

The measurements of the present work reveal also that, even though the increased crossover, the ohmic resistance, measured as HFR from impedance spectra, is not modified with ageing. Its value

(Figure 4.D and Figure SI-3**)** does not change between BoT and EoT, staying close to 26-28 mΩ $cm^{-2}$. The same conclusion is drawn for the other spectra obtained during intermediate long stops (data not reported).

SEM images of Figure 4.B reveal localized PEM deformation after the load cycle application, probably more pronounced under the ribs (Figure SI-4), as well as the presence of cracks into the electrodes. The very localized thinning is consistent to the increase in crossover current measured for CCM B (+30-40%) and related to diffusive hydrogen flux. The reduced CCM section might be connected to the presence of graphitic plates in the microporous layer (MPL) which, since in contact with the electrodes, seem to deform the CCM. The interplay between the components was verified preparing some *post-mortem* samples without removing the GDL before the epoxy embedding (Figure SI-5). The deformation is widespread along the flow field: the structural alterations look the result of mechanical stress, as could be inferred from irregularities, that are responsible for local thinning as for increased PEM sections nearby, denoting a structural re-arrangement that led even to failure in case of CCM A.

To summarize, dynamic automotive-like conditions reduce stability of membranes and resulted as a material-specific and time-dependent phenomenon, challenging even in case of robust component design. The regions that are stressed by fluctuations in water state due to dynamics, high humidification and relatively higher currents, as the air middle portion, appear more prone to the occurrence of membrane pinholes and micro-cracks. It should be noted that OCV, recognized to enhance the formation of peroxide and radical species which chemically attack PFSA[64], is avoided in the present protocol, as in the applications. The results suggest that the mechanical fatigue has a key role. However, synergistic effects between mechanical and chemical degradation could subsist. Few works[63] proved that membranes are subjected to depletion of cerium, used as radical scavenger, in the region most stressed mechanically because of the strongest water fluxes. The migration of the radical scavenger might promote chemical issues at the location where the mechanical fatigue is intense; such an effect cannot be excluded in this work as well.

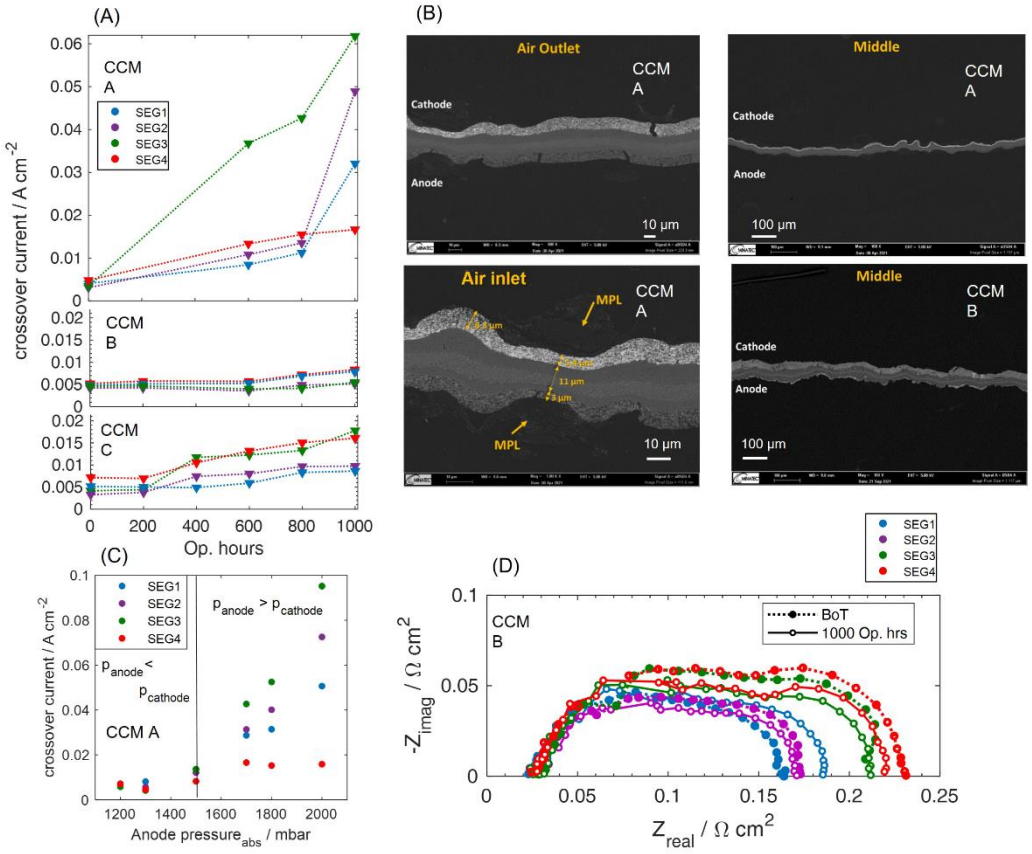


*Figure 4 (A) Local crossover current measured through Linear Sweep Voltammetry at 80 °C, $H_2/N_2$ flux = 300/300 ml $min^{-1}$ $p_{anode,\,in}$ = 1500 mbar, $p_{cathode,\,out}$ = ambient pressure. Crossover current density is reported as a function of the operating hours and measured during long stop characterization; (B) SEM images of CCM A at different locations along the flow field and CCM B in the middle area. Membrane and catalyst layer deformation is visible, as induced by the driving cycle protocol application. Deformed regions with a reduced thickness seem connected to MPL graphitic plates; (C) Local crossover current measured through Linear Sweep Voltammetry at 80 °C, $H_2/N_2$ flux = 300/300 ml $min^{-1}$, $p_{cathode,\,in}$ = 1500 mbar while varying $p_{anode,in}$., measured at 1000 operating hours of load cycle protocol; (D) Local Nyquist plots recorded at BoT and at 1000 operating hours of load cycle protocol for reference polarization curve conditions, at overall drawn current density equal to 0.8 A $cm^{-2}$.*

### *3.4. Catalyst layer: additional irreversible losses*

This section focuses on the additional degradation mechanisms of the cathode catalyst layer not described previously.

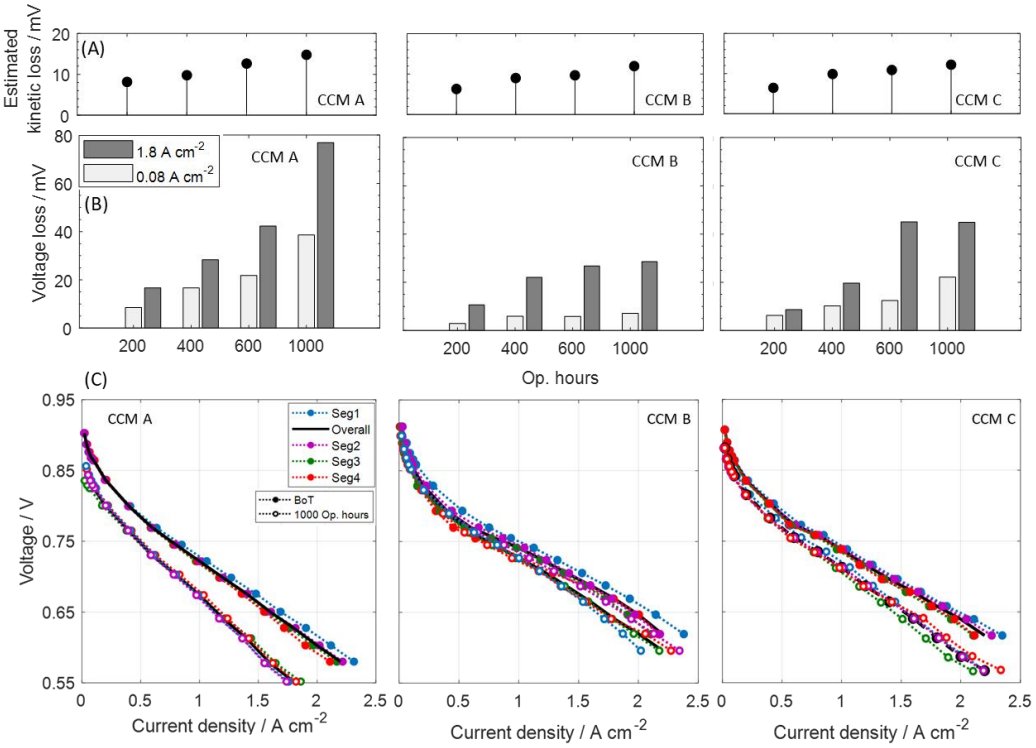


*Figure 5 (A) Pure kinetic loss estimated from ECSA loss by assuming a simple Tafel model for ORR, as described by Equation 7; (B) Voltage loss computed as difference between global performance at aged state and BoT, measured under reference polarization curve conditions (Table 2). Evolution as a function of operating hours is reported at the two selected current densities of 0.08 A cm$^{-2}$ and 1.8 A cm$^{-2}$; (C) Reference polarization curves: global(black) and local (coloured) performance are compared at BoT and after 1000 operating hours of load cycle protocol.*

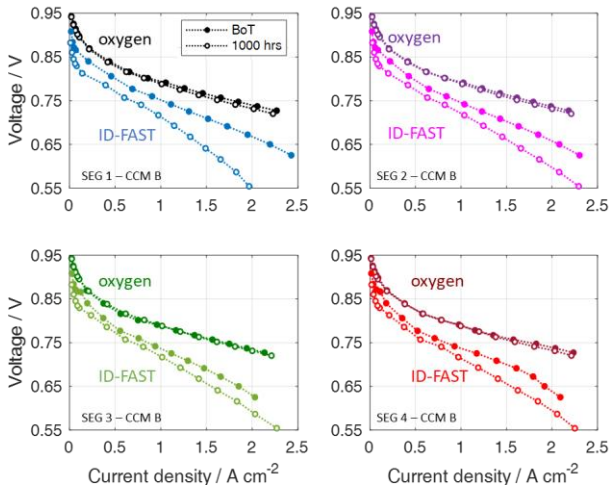


*Figure 6 CCM B performance: oxygen and ID-FAST polarization curves (Table 2) are reported, in dark and light colours respectively. Local performance of each segment is compared at BoT (full dots) and after 1000 operating hours of load cycle protocol (empty dots).*

*Table 8 Voltage loss computed as difference between performance at 1000 operating hours and BoT. Values are reported for two specific current densities and for the different polarization curves operating conditions. Both local polarization curves (i.e. related to segments 1-4) and global performance (overall) have been considered.*

| **CCM A:** local and overall voltage losses (mV) after 1000 operating hours | | | | | | |
|---|---|---|---|---|---|---|
| | Oxygen polarization curve | | Reference polarization curve | | ID-FAST polarization curve | |
| CCM region | *0.08 A cm$^{-2}$* | *1.8 A cm$^{-2}$* | *0.08 A cm$^{-2}$* | *1.8 A cm$^{-2}$* | *0.08 A cm$^{-2}$* | *1.8 A cm$^{-2}$* |
| *Seg 1* | 20 | 45 | 31 | 93 | 51 | 108 |

| | | | | | | |
|---|---|---|---|---|---|---|
| *Seg 2* | 21 | 43 | 35 | 87 | 50 | 90 |
| *Seg 3* | 31 | 30 | 47 | 64 | 51 | 60 |
| *Seg 4* | 22 | 37 | 35 | 62 | 46 | 56 |
| *Overall* | 25 | 38 | 39 | 76 | 50 | 74 |
| **CCM B:** local and overall voltage losses (mV) after 1000 operating hours | | | | | | |
| | Oxygen polarization curve | | Reference polarization curve | | ID-FAST polarization curve | |
| CCM region | *0.08 A cm$^{-2}$* | *1.8 A cm$^{-2}$* | *0.08 A cm$^{-2}$* | *1.8 A cm$^{-2}$* | *0.08 A cm$^{-2}$* | *1.8 A cm$^{-2}$* |
| *Seg 1* | 6 | 9 | 23 | 52 | 29 | 69 |
| *Seg 2* | 5 | 6 | 8 | 10 | 32 | 61 |
| *Seg 3* | 4 | 4 | -2 | 22 | 34 | 40 |
| *Seg 4* | 0.06 | 7 | 8 | 45 | 36 | 55 |
| *Overall* | 5 | 6 | 7 | 27 | 33 | 57 |
| **CCM C:** local and overall voltage losses (mV) after 1000 operating hours | | | | | | |
| | Oxygen polarization curve | | Reference polarization curve | | ID-FAST polarization curve | |
| CCM region | *0.08 A cm$^{-2}$* | *1.8 A cm$^{-2}$* | *0.08 A cm$^{-2}$* | *1.8 A cm$^{-2}$* | *0.08 A cm$^{-2}$* | *1.8 A cm$^{-2}$* |
| *Seg 1* | 5 | 28 | 23 | 53 | 33 | 77 |
| *Seg 2* | 11 | 28 | 22 | 41 | 38 | 61 |
| *Seg 3* | 5 | 22 | 22 | 38 | 45 | 76 |
| *Seg 4* | 5 | 12 | 22 | 41 | 34 | 40 |
| *Overall* | 7 | 23 | 22 | 45 | 35 | 60 |

The reference polarization curve (defined in Table 2) is selected to evidence the differences in performance among the CCMs. Figure 5.C depicts the overall (cell average) and local i-V curves at BoT and after 1000 operating hours of the load cycle. Average loss is consistent with the *operando* decay: CCM A evidences the largest losses, showing a large impact at low current densities, penalized because of the membrane ageing described in the previous section. CCM B is the most performant in the end, while, in comparison, CCM C is subjected to a larger decay at intermediate/high currents. The average evolution is detailed in Figure 5.B, where changes in time at two selected low (0.08 A cm$^{-2}$) and high (1.8 A cm$^{-2}$) currents are provided. CCM B reveals larger losses in the first 400 hours, after which variations are minor. The trend is coherent to Pt active surface area decay (Figure 3.A). The purely kinetic performance loss could be predicted considering Tafel kinetics for ORR[8]. Under the hypothesis that the reference exchange current density is not varying in time, the overpotential variation is estimated as:

$$\Delta\eta_{ORR} = \frac{2.303 \cdot RT}{\alpha F} \cdot log\left(\frac{ECSA_{BoT}}{ECSA_{cycle}}\right) \quad (7)$$

Where $ECSA_{cycle}$ indicates the ECSA at a specific cycle of the protocol, while $\alpha$ is the anodic transfer coefficient, set equivalent to 1[65]. Kinetics losses calculated according to Equation 7 are included

in Figure 5.A. CCM B shows, at low currents, a performance decay very close to such estimation. Discrepancies, in particular experimental values that are 2÷4 mV lower than theoretical, are attributed to measurement uncertainty or to limitations in this simple model. Both progression and stabilization are similar for CCM C voltage loss at 0.08 A $cm^{-2}$, deviating compared to CCM B only at the end of the test, where the larger increase of crossover current, that becomes ~2.6 times larger than BoT, probably boost the low load decline.

It is well known that mass transport losses promote an additional decreases of performance at high current densities [66]. For CCM B, the voltage loss at 1.8 A $cm^{-2}$ (Figure 5.B) follows, again, the ECSA evolution and the difference respect to the low current could be largely attributed to gas transport limitations, which grow at increasing values of geometric current densities, *i.e.* at increasing ratio $i_{geo}[\,A\,cm^{-2}]\,/\,ECSA$[67]. CCM C is subjected to an incentivized high current degradation, mostly from 600 hours, a behaviour that diverges from CCM B and hints to more intensified ageing mechanisms that would differ from Pt active area drop because of Pt NP increase in size only. Finally, CCM A shows no stabilization, as evinced from the *operando* voltage also. Membrane failure could promote additional ageing phenomena[68] (*e.g.* due to high local temperature because of direct reaction between hydrogen crossover and oxygen) that make the trend of irreversible losses significantly vary compared to other MEAs.

For all the materials, the distribution of local polarization curves at EoT differs from BoT (Figure 5.C). The polarization curve of segment 1, that was the best performing at the beginning, dropped down to provide a lower EoT contribution. The result is coherent to the irreversible re-distribution of local currents described in the *operando* analysis. The same information is evinced by the losses included in Table 8: segment 1 shows at 1.8 A $cm^{-2}$ a voltage drop that is ~8-25 mV larger than the overall loss, under reference conditions. Air inlet loses thus 20%-90% more than the CCM average at high current density.

In all the regions, the voltage drops of Table 8 are higher under air rather than pure oxygen (reference *vs* oxygen polarization curve) and even more promoted at ID-FAST conditions, characterized by lower relative humidity and temperature, while higher pressure (ID-FAST *vs* reference polarization curve). Different local i-V curves of CCM B are also compared in Figure 6. Results suggest that the same MEA local aged state leads to a different performance decay under various operating conditions, meaning that the loss could be stressed or attenuated acting on specific parameters like oxygen concentration and relative humidity. The reduction of these two quantities was proved to be detrimental, mostly for the air-inlet. Segment 1 suffers at medium-high currents: at 1.8 A $cm^{-2}$, EoT performance at ID-FAST conditions is 15-24 mV lower than reference case.

To investigate the origin of the additional losses evinced through polarization curves, the mass transport resistance was evaluated through the limiting current measurement. Figure 7.A illustrates the dependence of $R_{MT}$ on cathode pressure, at each long stop. Linear fitting at BoT and at 1000 hours was included. CCM B behaviour is clearly unchanged in pressure dependence: the slope of the fitting curve is unvaried over time, meaning that only the pressure independent contribution increased. Since the transport resistance related to intermolecular gas diffusion[69] is kept unchanged, it is concluded that GDL is not undergoing significant modifications. The mass transport resistance of CCM B was then plotted as a function of the inverse of roughness factor (*rf*), that expresses the ratio between the catalyst and the geometric electrode active area. The *rf* is the product of the catalyst loading and of Pt active surface area and its value changes with the load cycle application because of ECSA decrease. Greszler et al.[70] found that a reduction of Pt surface due to electrochemical Ostwald ripening mechanism results in an increasing mass transport close to a reduced catalyst loading, *i.e.* the surface resistance becomes more relevant due to reactant flux concentration. In their paper, the adoption of a graphitized catalyst support led to resistance values comparable to ones of CCM B. They also found a chart slope, reasonably representing local thin-film resistance, in range 12-14 s $cm^{-1}$. The linear dependence is proved in the present work as well (Figure 7.B), with a slope of 15-17 s $cm^{-1}$. As a conclusion, the driving cycle protocol caused a decay in the oxygen transport properties of CCM B that is mainly driven by particle size increase. The slightly higher values could be explained by analyzing what happens locally. In Figure 7.C, the segments contribution to the overall limiting current is provided over time. Segment 1 results as more degraded than others, since it decreases the relative current provided during the limiting current density test: $i_{share,1}$ irreversibly decreases from 1.41 to 1.30, while other $i_{share,j}$ are almost unchanged, as if the air-inlet resistance increases more than average. Since this variation is pressure independent (Figure SI-6), it could be imagined an alteration of the thin-film resistance or of the microporous catalyst layer structure. This impact is suspected to be more on gas transport rather than proton transport properties, at least at fully humidified conditions, as deduced from minor changes of impedance spectra in hydrogen/nitrogen (Figure SI-7). It is speculated that the drier inlet region not only suffers more because of reversible ageing, but it also undergoes some irreversible degradation in the local transport, consistently to the uneven performance losses observed under different polarization curves conditions at middle-high currents, previously described. Indeed, mass transport limitations become more evident at lower oxygen partial pressure and lower relative humidity (Table 8, Figure 5.C and Figure 6). The irreversible alteration of air-inlet region might be attributed to (*i*) the combination of dry low load operation and wide humidification cycles over one-hour protocol (impedance of Figure 1.B), that could cause loss and redistribution (adhesion) of the ionomer within the catalyst layer, as observed after 1100 h operation

by Morawietz et al.[71]; (*ii*) irreversible decomposition of the sulfonate groups near catalyst surface, promoted at low relative humidity, as in Isegawa et al. work[72].

For CCM C, trend and intensity of performance losses partially differ from CCM B and could be correlated to a larger increase of oxygen transport resistance: even though the catalyst of this MEA appears as more performant in limiting current conditions at BoT, the progressive evolution of $R_{MT}$ indicates more intensified ageing processes that occur within the catalyst layer, as observed from the larger slope of Figure 7.B, which is 35 – 40 s cm$^{-1}$, almost three times larger than other samples. Local analysis of CCM C, in Figure 7.C, confirms what described for the air-inlet of CCM B, even though the local re-distribution is less evident in this second case ($i_{share,1}$ drops from 1.47 to 1.42). The trend of CCM C resistance well correlates to the larger losses of performance observed in polarization curves of Figure 5.C, mostly in the high-currents range: this could be explained, at least in part, by alterations of the local resistance, related to the ionomer thin-film. A limitation of the transport mechanisms is expected to highly impact on the dynamic performance of the drive load cycle because its operating conditions, like low stoichiometry and low relative humidity, could incentivize the performance loss. CCM C *operando* voltage loss at the maximum load is strongly negatively affected, reaching a degradation rate of 136.1 µV h$^{-1}$, much higher than CCM B observations. Finally, the CCM A trend of Figure 7.B is quite aligned to CCM B; the reader is advised that mass transport resistance values are not reported in this chart after failure, while they are included in Figure 7.A, since mass transport determination is less reliable.

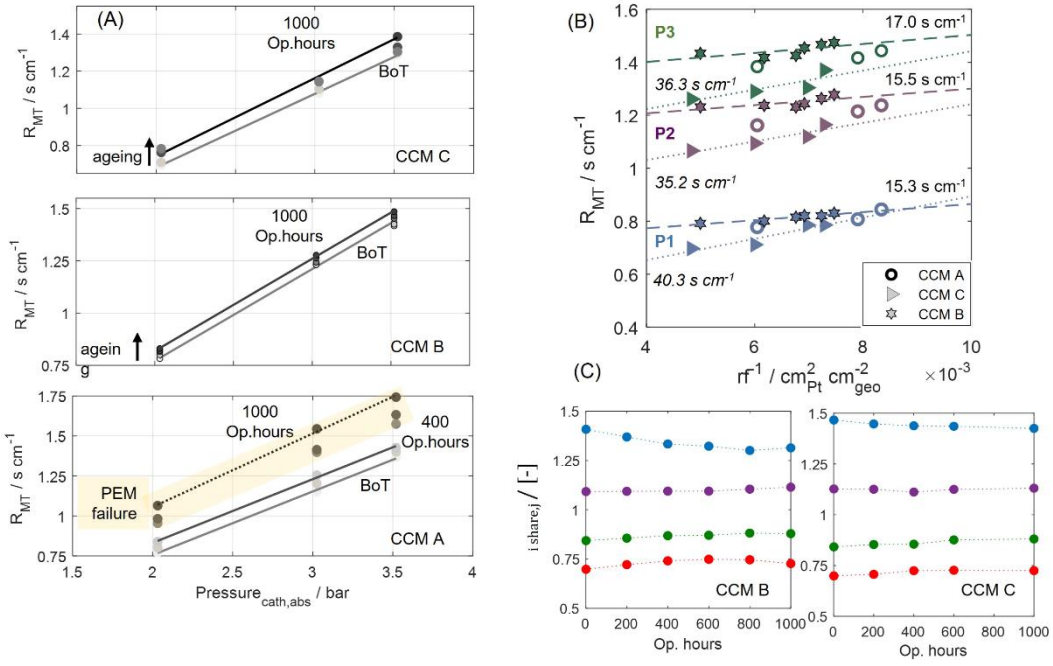


*Figure 7 (A) Total oxygen mass transport resistance ($R_{MT}$) as function of the absolute cathode pressure. Measurement is carried out at long stops, every 200$^{th}$ cycles. A chart is reported for each tested CCM; (B) Total overall oxygen mass transport resistance ($R_{MT}$) as function of the inverse of the roughness factor, where the roughness factor is progressively decreasing as consequence of the degradation caused by the load cycle protocol application. Linear fitting is reported for CCM B (dashed line) and CCM C (dotted line). For CCM A values are included up to 400 operating hours: from 600 hours membrane failure was detected, making unreliable*

*the measurement of $R_{MT}$ (large increase is observed in Figure 7.A); (C) Specific current density fraction of the overall limiting current, computed according to Equation 1. The evolution of each segment contribution is reported as a function of the operating hours.*

### *3.5. Influence of degradation mechanisms on cycle efficiency*

In the following, it is presented how the degradation phenomena impact on cycle efficiency. The cycle efficiency is a parameter that provides a broad picture of the MEA decay, computed as an energy efficiency according to Equation 8. It is the ratio of the output energy to the lower heating value of the input hydrogen, consumed in order to draw the current setpoint. This evaluation is done over one cycle of the protocol, by data registered every second:

$$\eta = \frac{\int \Delta V \; i \; dt}{\int \frac{i}{2F} M_m^{H2} dt \; \cdot LHV_{H2}} \qquad (8)$$

where $\Delta V$ corresponds to the operando cell voltage, $i$ is the current density, $M_m^{H2}$ is the hydrogen molar mass and $LHV_{H2}$ is the Lower Heating Value of hydrogen. The resulting values are in Figure 8. The trends of Figure 8 are consistent to the *operando* voltage losses of Figure 2.A. However, compared to current-specific voltages, the efficiency parameter combines in a weighted average the various setpoints encompassed during operation providing thus a representative picture of the whole automotive driving. It also allows to compare operational modes, as the low load and the high load functioning, that by nature include many operational setpoints. This partial information is quantified, again, through Equation 8 but limiting the integrals just to the low and to the high load part of each protocol cycle, according to the cycle separation provided in Figure 1.A and explained in Section 2.6. As evinced by the profiles, high load has the major impact on the overall cycle efficiency.

BoT cycle efficiencies are collected in Table 9. Low load efficiency is the same for all the CCMs (*i.e.* 63%, with an instantaneous peak efficiency[73] attained to 67%) while high load ranges between 51-54%: the combination of the two operations results in an overall efficiency of 54-56%.

The application of the ageing protocol comprises two types of losses, reversible and irreversible, as already described. The reversible degradation recovered during long stops permitted to increase of ~1-2% the efficiency in case of CCM A and B, while CCM C do not show variations. The recovery of reversible effects is more pronounced in the first 200-400 cycles, after which the contribution becomes <1%.

Overall cycle efficiency decreases of ~3% for CCM B. The decrease of efficiency is comparable at low load (~2%) and high load conditions (~3%). The trend results from the described dominating electrochemical Ostwald ripening mechanism: the larger losses at higher current density could be attributed to mass transport limitations that rise because of ECSA loss and to a probable degradation of ionomer in the air-inlet region of cathode catalyst layer.

Efficiency loss is larger for CCM A: an overall ~9% decrease was quantified. Separating the cycle into the two types of operation, a loss of ~5% is attributed to low load while of ~11% to the high load functioning. CCM A shows a larger impact in low load operation than the other samples since PEM failure (~10 times larger hydrogen crossover current at EoT compared to BoT).

An overall loss of ~9% was registered for CCM C. Even though this result is close to CCM A, the observed partial information differs. Low load degradation is comparable to CCM B (~3%) and is dominated by an analogous ECSA decay. On the other hand, significant deviations are registered for high load, that reduced its efficiency of ~12%. These results are consequence of the observed much more accelerated rate of decay of transport limitations in the cathode catalyst layer, due to either proton or gas transport phenomena (see Table 8 and Figure 7, previously described).

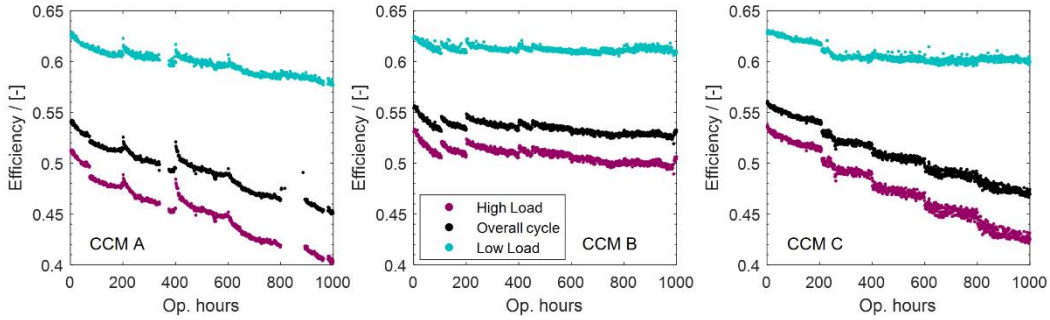


*Figure 8 Cycle efficiency of each tested CCM evaluated as a function of operating hours. Efficiency is evaluated according to Equation 8. Overall cycle is compared against low load and high load operation, defined as included in the load cycle protocol section.*

*Table 9 Cycle efficiency at BoT and at EoT, i.e. at 1000 operating hours, for each tested CCM. Overall cycle efficiency is included, as well as low load and high load efficiencies.*

| | **CCM A** | | **CCM B** | | **CCM C** | |
|---|---|---|---|---|---|---|
| | *BoT* | *EoT* | *BoT* | *EoT* | *BoT* | *EoT* |
| Overall cycle efficiency [%] | 54 | 45 | 56 | 53 | 56 | 47 |
| Low Load cycle efficiency [%] | 63 | 58 | 63 | 61 | 63 | 60 |
| High Load cycle efficiency [%] | 51 | 40 | 53 | 50 | 54 | 42 |

## 4. Conclusions

This work shows the results of a degradation testing program designed to mimic automotive driving in a comprehensive way. Local effects were studied through a segmented hardware, evidencing the role of ageing mechanisms in relation to heterogeneous operating conditions. A meaningful ageing experiment was performed on a single fuel cell with the objective of including vehicle-like operations. The load cycle protocol, designed from a customer fleet dataset, included

temperature ramps and cycles of gas feeding humidification, pressure and load. Main findings are summarized:

*(i)* different stop conditions were reproduced, to stay close to real-world: the introduction of short stops and cold soaks allow to recover part of reversible degradation, thanks to platinum oxides removal and re-humidification. Further reversible losses were removed at long stops: being for longer times at ambient temperature and applying a suitable cathode catalyst cleaning procedure allowed for an additional recovery, probably connected to ionomer. The extent of reversible losses is material dependent: the performance improves from few to ~20 mV. The effect is more pronounced at air-inlet and at low current densities, possibly since the driest operating conditions of this MEA portion. After long stop, local current contribution is recovered: $i_{share,1}$ increases even from ~0.40 to ~0.70 at the lowest load;

*(ii)* irreversible ageing was proved due to cathode catalyst layer and membrane degradation. All these mechanisms caused a cycle efficiency loss from ~3% to ~9%. The larger loss is at high load operation (~3%-12%), while lower at low load (~3%-5%). Consistently, the rate of voltage decay increases with the current setpoint;

*(iii)* Electrochemical Ostwald ripening mechanism is the main mechanism regarding catalyst at the cathode electrode: increase in particle size is aligned to ECSA decay, while no signs of Pt band formation and carbon support corrosion were evinced. The largest variation of ECSA is within the first 200/400 operating hours. Evolutions are similar for all the materials, with a final value that is 62%-67% of BoT;

*(iv)* membrane degradation resulted as mechanically driven, consequence of the stress due to dynamic operations, that impact on ionomer humidification state. PFSA membranes, even though all reinforced and chemically stabilized, were characterized by different durability: CCM A failed because of pinhole formation, increasing the hydrogen crossover current by a factor ~10, responsible of large performance drops at low current. This material did not show a stabilization of the performance decay, probably because the defect drew additional degradation processes. CCM B showed much more limited variations in crossover current (factor ~1.4), attributed to localized membrane thinning. Interestingly, the middle/close-to-outlet region (segment 3) resulted in general as the most susceptible to membrane ageing;

*(v)* irreversible performance losses are largely justified by ECSA decay for CCM B, as the increase in mass transport resistance, that showed a linear dependence on the inverse of roughness factor, with a slope of 15-17 s $cm^{-1}$. On the contrary, CCM C showed boosted

decay from 600 operating hours that are attributed to more promoted alterations within the catalyst layer and to different material properties: the mass transport resistance increases ~2.5 times more than CCM B, negatively impacting on the high current operation of the load cycle (at the two highest currents, the degradation rates are 43.3 μV $h^{-1}$ and 136.1 μV $h^{-1}$ for CCM C against 21.9 μV $h^{-1}$ and 31.7 μV $h^{-1}$ for CCM B);

*(vi)* irreversible ageing was heterogeneous in the along-the-flow-field direction. Air-inlet suffered the largest performance losses, an effect more evident under operating conditions that stress transport limitations (low oxygen partial pressure and low relative humidity). EoT segment 1 performance loss at ID-FAST conditions is 15-24 mV higher than at reference operating parameters, that is, in turn, 25-48 mV higher than under oxygen feeding. The observation is confirmed through the local analysis of the limiting current measurement: the higher local impact might be related to a larger increase in the local thin-film resistance. Note that heterogeneities were detected in GSA and ECSA too. Larger particles are at air-outlet, because of the higher humidification, while distribution is slightly shifted towards smaller diameters at the drier inlet, proving that the locally decreased limiting current at air-inlet could not be explained by Pt active area loss only, but structural changes of ionomer should subsist.

At high currents, performance decay is instead lower in the air-middle, that seems more affected by membrane but less by catalyst layer degradation: the performance of this region compensates the losses of the others, as evinced by local current distribution.

## Appendix

In the following, a more detailed description of the procedures adopted for the testing protocol is provided.

*Short stop*

The short stop procedure is frequently introduced in the protocol (twice per operating hour) in order to mimic the frequent interruptions that are expected in a real application: very rarely the vehicle is operated for many hours without stopping. Short stop protocol for single cell testing consists in the steps:

- A clipping voltage equal to 0.85 V is set;
- Gas flows are reduced to the minimum (stoichiometric flow rate equivalent to 0.2 A $cm^{-2}$);
- Gas pressures are reduced to ambient value;
- Hydrogen flow is still supplied at the anode side while air flow is stopped;
- Cell voltage is let decrease to values < 0.1 V, condition kept for 5 minutes;

- Cell temperature is not reduced (no cooling down).

*Cold soak*

The cold soak protocol would like to reproduce the regular stops in real systems that are long enough to cause the complete cooling down. Cold soaks are less frequent rather than short stops. In particular, a cold soak is introduced every 5 operating hours. For the present work about single cell testing, cold soak is performed as:

- A clipping voltage equal to 0.85 V is set;
- Gas flows are reduced to a minimum (stoichiometric flow rate equivalent to 0.2 A $cm^{-2}$);
- Gas pressures are reduced to ambient value;
- Hydrogen flow is still supplied at the anode side while at the cathode side the flow is switched from air to nitrogen;
- Cell voltage is let decrease to values < 0.1 V, under an inert atmosphere, in the meanwhile temperature control is turned off;
- Condition is kept for 2 hours.

*Long stop*

The long stop mimics a situation in which the vehicle is turned off for several days. It is expected to be a rare event, therefore introduced every 200 operating hours. For the present work about single cell testing, the procedure adopted is equivalent to cold soak, but the stop lasts for 12 hours. Thereafter, the cathode recovery procedure is performed. It consists in performing cyclic voltammetry between 0.07 – 1.20 VRHE for 10 times, with a scan rate of 100 mV $s^{-1}$ at 30 °C and outlet ambient pressure. The anode is fed with fully humidified 0.06 NL $min^{-1}$ hydrogen, while the cathode is fed with 0.06 NL $min^{-1}$ nitrogen.

## CRediT authorship contribution statement

**Elena Colombo:** Methodology, Conceptualization, Investigation, Formal analysis, Data curation, Writing - Original Draft;
**Andrea Baricci:** Methodology, Conceptualization, Writing - Review & Editing;
**Andrea Bisello:** Methodology;
**Laure Guetaz:** Investigation, Writing - Review & Editing;
**Andrea Casalegno:** Supervision, Project administration.

## Acknowledgments

This project has received funding from the Fuel Cells and Hydrogen 2 Joint Undertaking under grant agreement No 779565 (ID-Fast)**.** This Joint Undertaking receives support from the European Union's Horizon 2020 research and innovation program**.**

**References**

[1] https://www.fch.europa.eu/soa-and-targets, (2021).

[2] J. Zhao, X. Li, A review of polymer electrolyte membrane fuel cell durability for vehicular applications: Degradation modes and experimental techniques, Energy Convers. Manag. 199 (2019) 112022. https://doi.org/10.1016/j.enconman.2019.112022.

[3] P. Ren, P. Pei, Y. Li, Z. Wu, D. Chen, S. Huang, Degradation mechanisms of proton exchange membrane fuel cell under typical automotive operating conditions, Prog. Energy Combust. Sci. 80 (2020) 100859. https://doi.org/10.1016/j.pecs.2020.100859.

[4] S. Stariha, N. Macauley, B.T. Sneed, D. Langlois, K.L. More, R. Mukundan, R.L. Borup, Recent Advances in Catalyst Accelerated Stress Tests for Polymer Electrolyte Membrane Fuel Cells, J. Electrochem. Soc. 165 (2018) F492–F501. https://doi.org/10.1149/2.0881807jes.

[5] R.L. Borup, A. Kusoglu, K.C. Neyerlin, R. Mukundan, R.K. Ahluwalia, D.A. Cullen, K.L. More, A.Z. Weber, D.J. Myers, Recent developments in catalyst-related PEM fuel cell durability, Curr. Opin. Electrochem. 21 (2020) 192–200. https://doi.org/10.1016/j.coelec.2020.02.007.

[6] Y. Shao-Horn, W.C. Sheng, S. Chen, P.J. Ferreira, E.F. Holby, D. Morgan, Instability of supported platinum nanoparticles in low-temperature fuel cells, Top. Catal. 46 (2007) 285–305. https://doi.org/10.1007/s11244-007-9000-0.

[7] R.K. Ahluwalia, X. Wang, J.-K. Peng, V. Konduru, S. Arisetty, N. Ramaswamy, S. Kumaraguru, Achieving 5,000-h and 8,000-h Low-PGM Electrode Durability on Automotive Drive Cycles, J. Electrochem. Soc. 168 (2021) 044518. https://doi.org/10.1149/1945-7111/abf507.

[8] P. Zihrul, I. Hartung, S. Kirsch, G. Huebner, H.A. Gasteiger, Voltage Cycling Induced Losses in Electrochemically Active Surface Area and in H 2 / Air-Performance of PEM Fuel Cells, 163 (2016) 492–498. https://doi.org/10.1149/2.0561606jes.

[9] A. Kneer, A Semi-Empirical Catalyst Degradation Model Based on Voltage Cycling under Automotive Operating Conditions in PEM Fuel Cells, 166 (2019) 120–127. https://doi.org/10.1149/2.0641902jes.

[10] C. Takei, K. Kakinuma, K. Kawashima, K. Tashiro, M. Watanabe, M. Uchida, Load cycle durability of a graphitized carbon black-supported platinum catalyst in polymer electrolyte fuel

cell cathodes, J. Power Sources. 324 (2016) 729–737. https://doi.org/10.1016/j.jpowsour.2016.05.117.

[11] A. Kneer, N. Wagner, C. Sadeler, A. Scherzer, D. Gerteisen, Effect of Dwell Time and Scan Rate during Voltage Cycling on Catalyst Degradation in PEM Fuel Cells, 165 (2018) 805–812. https://doi.org/10.1149/2.0651810jes.

[12] K. Yu, D.J. Groom, X. Wang, Z. Yang, M. Gummalla, S.C. Ball, D. Myers, P.J. Ferreira, Degradation mechanisms of platinum nanoparticle catalysts in proton exchange membrane fuel cells: The role of particle size, Microsc. Microanal. 20 (2014) 482–483. https://doi.org/10.1017/S1431927614004139.

[13] T.E. O'Brien, S. Herrera, D.A. Langlois, N.N. Kariuki, H. Yu, M.J. Zachman, D.J. Myers, D.A. Cullen, R.L. Borup, R. Mukundan, Impact of Carbon Support Structure on the Durability of PtCo Electrocatalysts, J. Electrochem. Soc. 168 (2021) 054517. https://doi.org/10.1149/1945-7111/abfe46.

[14] R. Mukundan, A.M. Baker, A. Kusoglu, P. Beattie, S. Knights, A.Z. Weber, R.L. Borup, Membrane Accelerated Stress Test Development for Polymer Electrolyte Fuel Cell Durability Validated Using Field and Drive Cycle Testing, J. Electrochem. Soc. 165 (2018) F3085–F3093. https://doi.org/10.1149/2.0101806jes.

[15] P.C. Okonkwo, I. Ben Belgacem, W. Emori, P.C. Uzoma, Nafion degradation mechanisms in proton exchange membrane fuel cell (PEMFC) system: A review, Int. J. Hydrogen Energy. 46 (2021) 27956–27973. https://doi.org/10.1016/j.ijhydene.2021.06.032.

[16] X. Sun, S. Shi, Y. Fu, J. Chen, Q. Lin, J. Hu, C. Li, J. Li, X. Chen, Embrittlement induced fracture behavior and mechanisms of perfluorosulfonic-acid membranes after chemical degradation, J. Power Sources. 453 (2020) 227893. https://doi.org/10.1016/j.jpowsour.2020.227893.

[17] A. Kusoglu, A.M. Karlsson, M.H. Santare, S. Cleghorn, W.B. Johnson, Mechanical response of fuel cell membranes subjected to a hygro-thermal cycle, J. Power Sources. 161 (2006) 987–996. https://doi.org/10.1016/j.jpowsour.2006.05.020.

[18] Q. Lin, S. Shi, L. Wang, X. Chen, G. Chen, Biaxial fatigue crack propagation behavior of perfluorosulfonic-acid membranes, J. Power Sources. 384 (2018) 58–65. https://doi.org/10.1016/j.jpowsour.2018.02.002.

[19] T. Morawietz, M. Handl, C. Oldani, P. Gazdzicki, J. Hunger, F. Wilhelm, J. Blake, K.A. Friedrich, R. Hiesgen, High-Resolution Analysis of Ionomer Loss in Catalytic Layers after Operation, J. Electrochem. Soc. 165 (2018) F3139–F3147. https://doi.org/10.1149/2.0151806jes.

[20] and Z. (Simon) L. Jian Zhao, Samaneh Shahgaldi, Xianguo Li, Experimental Observations of Microstructure Changes in the Catalyst Layers of Proton Exchange Membrane Fuel Cells under Wet-Dry Cycles, J. Electrochem. Soc. 165 (2018) F3337–F3345. https://doi.org/10.1146/annurev.matsci.33.022702.154657.

[21] J. Liu, Y. Yin, J. Zhang, T. Zhang, X. Zhang, H. Chen, Mechanical degradation of catalyst layer under accelerated relative humidity cycling in a polymer electrolyte membrane fuel cell, J. Power Sources. 512 (2021) 230487. https://doi.org/10.1016/j.jpowsour.2021.230487.

[22] S. Jomori, K. Komatsubara, N. Nonoyama, M. Kato, T. Yoshida, An Experimental Study of the Effects of Operational History on Activity Changes in a PEMFC, J. Electrochem. Soc. 160 (2013) F1067–F1073. https://doi.org/10.1149/2.103309jes.

[23] F. Du, T.A. Dao, P.V.J. Peitl, A. Bauer, K. Preuss, A.M. Bonastre, J. Sharman, G. Spikes, M. Perchthaler, T.J. Schmidt, A. Orfanidi, Effects of PEMFC Operational History under Dry/Wet Conditions on Additional Voltage Losses due to Ionomer Migration, J. Electrochem. Soc. 167 (2020) 144513. https://doi.org/10.1149/1945-7111/abc83f.

[24] L. Dubau, L. Castanheira, F. Maillard, M. Chatenet, O. Lottin, G. Maranzana, J. Dillet, A. Lamibrac, J.C. Perrin, E. Moukheiber, A. Elkaddouri, G. De Moor, C. Bas, L. Flandin, N. Caqué, A review of PEM fuel cell durability: Materials degradation, local heterogeneities of aging and possible mitigation strategies, Wiley Interdiscip. Rev. Energy Environ. 3 (2014) 540–560. https://doi.org/10.1002/wene.113.

[25] C. Rabissi, M. Zago, P. Gazdzicki, L. Guétaz, S. Escribano, L. Grahl-Madsen, A. Casalegno, A locally resolved investigation on direct methanol fuel cell uneven components fading: Local cathode catalyst layer tuning for homogeneous operation and reduced degradation rate, J. Power Sources. 404 (2018) 135–148. https://doi.org/10.1016/j.jpowsour.2018.09.094.

[26] D. Chen, P. Pei, Y. Li, P. Ren, Y. Meng, X. Song, Z. Wu, Proton exchange membrane fuel cell stack consistency: Evaluation methods, influencing factors, membrane electrode assembly parameters and improvement measures, Energy Convers. Manag. 261 (2022) 115651. https://doi.org/10.1016/j.enconman.2022.115651.

[27] Z. Hu, L. Xu, J. Li, Q. Gan, X. Xu, Z. Song, Y. Shao, M. Ouyang, A novel diagnostic methodology for fuel cell stack health: Performance, consistency and uniformity, Energy Convers. Manag. 185 (2019) 611–621. https://doi.org/10.1016/j.enconman.2019.02.031.

[28] C. Rabissi, M. Zago, L. Grahl-Madsen, M. Odgaard, A. Casalegno, Local durability optimization of a large-scale direct methanol fuel cell: catalyst layer tuning for homogeneous operation and in-operando detection of localized hydrogen evolution, J. Power Sources. 506 (2021) 230218. https://doi.org/10.1016/j.jpowsour.2021.230218.

[29] T. Lochner, L. Hallitzky, M. Perchthaler, M. Obermaier, J. Sabawa, S. Enz, A.S. Bandarenka, Local degradation effects in automotive size membrane electrode assemblies under realistic operating conditions, Appl. Energy. 260 (2020) 114291. https://doi.org/10.1016/j.apenergy.2019.114291.

[30] S. Enz, T.A. Dao, M. Messerschmidt, J. Scholta, Investigation of degradation effects in polymer electrolyte fuel cells under automotive-related operating conditions, J. Power Sources. 274 (2015) 521–535. https://doi.org/10.1016/j.jpowsour.2014.10.127.

[31] S. Abbou, J. Dillet, G. Maranzana, S. Didierjean, O. Lottin, Local potential evolutions during proton exchange membrane fuel cell operation with dead-ended anode – Part I: Impact of water diffusion and nitrogen crossover, J. Power Sources. 340 (2017) 337–346. https://doi.org/10.1016/j.jpowsour.2016.11.079.

[32] J. Durst, A. Lamibrac, F. Charlot, J. Dillet, L.F. Castanheira, G. Maranzana, L. Dubau, F. Maillard, M. Chatenet, O. Lottin, Degradation heterogeneities induced by repetitive start/stop events in proton exchange membrane fuel cell: Inlet vs. outlet and channel vs. land, Appl. Catal. B Environ. 138–139 (2013) 416–426. https://doi.org/10.1016/j.apcatb.2013.03.021.

[33] E. Colombo, A. Bisello, A. Casalegno, A. Baricci, Mitigating PEMFC Degradation During Start-Up: Locally Resolved Experimental Analysis and Transient Physical Modelling, J. Electrochem. Soc. 168 (2021) 054508. https://doi.org/10.1149/1945-7111/abf4eb.

[34] D.G. Sanchez, T. Ruiu, I. Biswas, M. Schulze, S. Helmly, K.A. Friedrich, Local impact of humidification on degradation in polymer electrolyte fuel cells, J. Power Sources. 352 (2017) 42–55. https://doi.org/10.1016/j.jpowsour.2017.03.057.

[35] D. Garcia-Sanchez, T. Morawietz, P.G. da Rocha, R. Hiesgen, P. Gazdzicki, K.A. Friedrich, Local impact of load cycling on degradation in polymer electrolyte fuel cells, Appl. Energy. 259 (2020) 114210. https://doi.org/10.1016/j.apenergy.2019.114210.

[36] D.G. Sanchez, J.E. Soc, D.G. Sanchez, T. Ruiu, K.A. Friedrich, J. Sanchez-monreal, M. Vera, Analysis of the Influence of Temperature and Gas Humidity on the Performance Stability of Polymer Electrolyte Membrane Fuel Cells Analysis of the Influence of Temperature and Gas Humidity on the Performance Stability of Polymer Electrolyte Membrane Fuel C, (2016). https://doi.org/10.1149/2.0071603jes.

[37] Y.H. Lai, G.W. Fly, In-situ diagnostics and degradation mapping of a mixed-mode accelerated stress test for proton exchange membranes, J. Power Sources. 274 (2015) 1162–1172. https://doi.org/10.1016/j.jpowsour.2014.10.116.

[38] Z. Hua, Z. Zheng, E. Pahon, M.C. Péra, F. Gao, A review on lifetime prediction of proton exchange membrane fuel cells system, J. Power Sources. 529 (2022).

https://doi.org/10.1016/j.jpowsour.2022.231256.

[39] M. Hasan, J. Chen, J.R. Waldecker, M.H. Santare, Predicting fatigue lifetimes of a reinforced membrane in polymer electrolyte membrane fuel cell using plastic energy, J. Power Sources. 539 (2022) 231597. https://doi.org/10.1016/j.jpowsour.2022.231597.

[40] D. Chen, P. Pei, Y. Meng, P. Ren, Y. Li, M. Wang, X. Wang, Novel extraction method of working condition spectrum for the lifetime prediction and energy management strategy evaluation of automotive fuel cells, Energy. 255 (2022) 124523. https://doi.org/10.1016/j.energy.2022.124523.

[41] ID-FAST - Investigations on degradation mechanisms and Definition of protocols for PEM Fuel cells Accelerated Stress Testing; Grant agreement no : 779565; Call : H2020-JTI-FCH-2017-1; D4 . 3 – Analysis of coupling between mechanisms and definition of comb, 2021.

[42] C. Rabissi, E. Brightman, G. Hinds, A. Casalegno, In operando measurement of localised cathode potential to mitigate DMFC temporary degradation, Int. J. Hydrogen Energy. 43 (2018) 9797–9802. https://doi.org/10.1016/j.ijhydene.2018.04.043.

[43] A. Bisello, E. Colombo, A. Baricci, C. Rabissi, L. Guetaz, P. Gazdzicki, A. Casalegno, Mitigated Start-Up of PEMFC in Real Automotive Conditions: Local Experimental Investigation and Development of a New Accelerated Stress Test Protocol, J. Electrochem. Soc. 168 (2021) 054501. https://doi.org/10.1149/1945-7111/abf77b.

[44] C. Rabissi, P. Gazdzicki, L. Guétaz, S. Escribano, L. Grahl-Madsen, A. Baricci, A. Casalegno, A locally resolved investigation on direct methanol fuel cell uneven components fading: Steady state and degradation local analysis, J. Power Sources. 397 (2018) 361–373. https://doi.org/10.1016/j.jpowsour.2018.07.034.

[45] D.R. Baker, D.A. Caulk, K.C. Neyerlin, M.W. Murphy, Measurement of Oxygen Transport Resistance in PEM Fuel Cells by Limiting Current Methods, J. Electrochem. Soc. 156 (2009) B991. https://doi.org/10.1149/1.3152226.

[46] P.J. Ferreira, G.J. la O', Y. Shao-Horn, D. Morgan, R. Makharia, S. Kocha, H.A. Gasteiger, Instability of Pt/C Electrocatalysts in Proton Exchange Membrane Fuel Cells, J. Electrochem. Soc. 152 (2005) A2256. https://doi.org/10.1149/1.2050347.

[47] J. Zhang, B.A. Litteer, F.D. Coms, R. Makharia, Recoverable Performance Loss Due to Membrane Chemical Degradation in PEM Fuel Cells, J. Electrochem. Soc. 159 (2012) F287–F293. https://doi.org/10.1149/2.063207jes.

[48] Q. Zhang, C. Harms, J. Mitzel, P. Gazdzicki, K.A. Friedrich, The challenges in reliable determination of degradation rates and lifetime in polymer electrolyte membrane fuel cells, Curr. Opin. Electrochem. 31 (2022) 100863. https://doi.org/10.1016/j.coelec.2021.100863.

[49] M. Zago, A. Baricci, A. Bisello, T. Jahnke, H. Yu, R. Maric, P. Zelenay, A. Casalegno, Experimental analysis of recoverable performance loss induced by platinum oxide formation at the polymer electrolyte membrane fuel cell cathode, J. Power Sources. 466 (2020). https://doi.org/10.1016/j.jpowsour.2020.228316.

[50] B.E. Conway, B. Barnett, H. Angerstein-Kozlowska, B. V. Tilak, A surface-electrochemical basis for the direct logarithmic growth law for initial stages of extension of anodic oxide films formed at noble metals, J. Chem. Phys. 93 (1990) 8361–8373. https://doi.org/10.1063/1.459319.

[51] P. Gazdzick, J. Mitzel, D. Sanchez, M. Schulze, K.A. Friedrich, Evaluation of reversible and irreversible degradation rates of polymer electrolyte membrane fuel cells tested in automotive conditions, J. Power Sources. 327 (2016) 86–95. https://doi.org/10.1016/j.jpowsour.2016.07.049.

[52] K. Kodama, R. Jinnouchi, T. Suzuki, H. Murata, T. Hatanaka, Y. Morimoto, Increase in adsorptivity of sulfonate anions on Pt (111) surface with drying of ionomer, Electrochem. Commun. 36 (2013) 26–28. https://doi.org/10.1016/j.elecom.2013.09.005.

[53] K. Shinozaki, Y. Morimoto, B.S. Pivovar, S.S. Kocha, Suppression of oxygen reduction reaction activity on Pt-based electrocatalysts from ionomer incorporation, J. Power Sources. 325 (2016) 745–751. https://doi.org/10.1016/j.jpowsour.2016.06.062.

[54] M.K. Debe, A.K. Schmoeckel, G.D. Vernstrom, R. Atanasoski, High voltage stability of nanostructured thin film catalysts for PEM fuel cells, 161 (2006) 1002–1011. https://doi.org/10.1016/j.jpowsour.2006.05.033.

[55] A.A. Topalov, S. Cherevko, A.R. Zeradjanin, J.C. Meier, I. Katsounaros, K.J.J. Mayrhofer, Chemical Science Towards a comprehensive understanding of platinum dissolution in acidic media, (2014) 631–638. https://doi.org/10.1039/c3sc52411f.

[56] T. Jahnke, A. Baricci, C. Rabissi, A. Casalegno, Physical Modeling of Catalyst Degradation in Low Temperature Fuel Cells: Platinum Oxidation, Dissolution, Particle Growth and Platinum Band Formation [ J. Electrochem. Soc. , 167 , 013523 (2020)], J. Electrochem. Soc. 167 (2020) 149001. https://doi.org/10.1149/1945-7111/abbfda.

[57] R.K. Ahluwalia, S. Arisetty, X. Wang, X. Wang, R. Subbaraman, S.C. Ball, S. Decrane, D.J. Myers, Thermodynamics and Kinetics of Platinum Dissolution from Carbon-Supported Electrocatalysts in Aqueous Media under Potentiostatic and Potentiodynamic Conditions, 160 (2013) 447–455. https://doi.org/10.1149/2.018306jes.

[58] H. Yu, A. Baricci, A. Bisello, A. Casalegno, L. Guetaz, L. Bonville, R. Maric, Strategies to mitigate Pt dissolution in low Pt loading proton exchange membrane fuel cell: I. A gradient Pt

particle size design, Electrochim. Acta. 247 (2017) 1155–1168. https://doi.org/10.1016/j.electacta.2017.07.093.

[59] K.H. Kangasniemi, D.A. Condit, T.D. Jarvi, Characterization of Vulcan Electrochemically Oxidized under Simulated PEM Fuel Cell Conditions, J. Electrochem. Soc. 151 (2004) E125. https://doi.org/10.1149/1.1649756.

[60] G.S. Harzer, J.N. Schwämmlein, A.M. Damjanović, S. Ghosh, H.A. Gasteiger, Cathode Loading Impact on Voltage Cycling Induced PEMFC Degradation: A Voltage Loss Analysis, J. Electrochem. Soc. 165 (2018) F3118–F3131. https://doi.org/10.1149/2.0161806jes.

[61] R.K.F. Della Bella, B.M. Stühmeier, H. Gasteiger, Universal Correlation between Cathode Roughness Factor and H 2 /Air Performance Losses in Voltage Cycling-Based Accelerated Stress Tests , J. Electrochem. Soc. (2022). https://doi.org/10.1149/1945-7111/ac67b8.

[62] S. Kreitmeier, M. Michiardi, A. Wokaun, F.N. Büchi, Factors determining the gas crossover through pinholes in polymer electrolyte fuel cell membranes, Electrochim. Acta. 80 (2012) 240–247. https://doi.org/10.1016/j.electacta.2012.07.013.

[63] Y.-H. Lai, K.M. Rahmoeller, J.H. Hurst, R.S. Kukreja, M. Atwan, A.J. Maslyn, C.S. Gittleman, Accelerated Stress Testing of Fuel Cell Membranes Subjected to Combined Mechanical/Chemical Stressors and Cerium Migration, J. Electrochem. Soc. 165 (2018) F3217–F3229. https://doi.org/10.1149/2.0241806jes.

[64] M.P. Rodgers, L.J. Bonville, H.R. Kunz, D.K. Slattery, J.M. Fenton, Fuel cell perfluorinated sulfonic acid membrane degradation correlating accelerated stress testing and lifetime, Chem. Rev. 112 (2012) 6075–6103. https://doi.org/10.1021/cr200424d.

[65] K.C. Neyerlin, W. Gu, J. Jorne, H.A. Gasteiger, Determination of Catalyst Unique Parameters for the Oxygen Reduction Reaction in a PEMFC, J. Electrochem. Soc. 153 (2006) A1955. https://doi.org/10.1149/1.2266294.

[66] A. Kongkanand, M.F. Mathias, The Priority and Challenge of High-Power Performance of Low-Platinum Proton-Exchange Membrane Fuel Cells, J. Phys. Chem. Lett. 7 (2016) 1127–1137. https://doi.org/10.1021/acs.jpclett.6b00216.

[67] J.P. Owejan, J.E. Owejan, W. Gu, Impact of Platinum Loading and Catalyst Layer Structure on PEMFC Performance, J. Electrochem. Soc. 160 (2013) F824–F833. https://doi.org/10.1149/2.072308jes.

[68] L. Guétaz, S. Escribano, O. Sicardy, Study by electron microscopy of proton exchange membrane fuel cell membrane-electrode assembly degradation mechanisms: Influence of local conditions, J. Power Sources. 212 (2012) 169–178. https://doi.org/10.1016/j.jpowsour.2012.03.096.

[69] N. Nonoyama, S. Okazaki, A.Z. Weber, Y. Ikogi, T. Yoshida, Analysis of Oxygen-Transport Diffusion Resistance in Proton-Exchange-Membrane Fuel Cells, J. Electrochem. Soc. 158 (2011) B416. https://doi.org/10.1149/1.3546038.

[70] T.A. Greszler, D. Caulk, P. Sinha, The Impact of Platinum Loading on Oxygen Transport Resistance, J. Electrochem. Soc. 159 (2012) F831–F840. https://doi.org/10.1149/2.061212jes.

[71] T. Morawietz, M. Handl, C. Oldani, P. Gazdzicki, J. Hunger, F. Wilhelm, J. Blake, K.A. Friedrich, R. Hiesgen, High-Resolution Analysis of Ionomer Loss in Catalytic Layers after Operation, J. Electrochem. Soc. 165 (2018) F3139–F3147. https://doi.org/10.1149/2.0151806jes.

[72] K. Isegawa, T. Nagami, S. Jomori, M. Yoshida, H. Kondoh, In situ S-K XANES study of polymer electrolyte fuel cells: Changes in the chemical states of sulfonic groups depending on humidity, Phys. Chem. Chem. Phys. 18 (2016) 25183–25190. https://doi.org/10.1039/c6cp04052g.

[73] https://www.energy.gov/eere/fuelcells/doe-technical-targets-fuel-cell-systems-and-stacks-transportation-applications.